

# Train Once, Deploy Anywhere: Realize Data-Efficient Dynamic Object Manipulation

Zhuoling Li, Xiaoyang Wu, Zhenhua Xu, Hengshuang Zhao

[https://lizhuoling.github.io/GEM\\_webpage](https://lizhuoling.github.io/GEM_webpage)

**Abstract**—Realizing generalizable dynamic object manipulation is important for enhancing manufacturing efficiency, as it eliminates specialized engineering for various scenarios. To this end, imitation learning emerges as a promising paradigm, leveraging expert demonstrations to teach a policy manipulation skills. Although the generalization of an imitation learning policy can be improved by increasing demonstrations, demonstration collection is labor-intensive. To address this problem, this paper investigates whether strong generalization in dynamic object manipulation is achievable with only a few demonstrations. Specifically, we develop an entropy-based theoretical framework to quantify the optimization of imitation learning. Based on this framework, we propose a system named Generalizable Entropy-based Manipulation (GEM). Extensive experiments in simulated and real tasks demonstrate that GEM can generalize across diverse environment backgrounds, robot embodiments, motion dynamics, and object geometries. Notably, GEM has been deployed in a real canteen for tableware collection. Without any in-scene demonstration, it achieves a success rate of over 97% across more than 10,000 operations.

**Index Terms**—Dynamic object manipulation, imitation learning, information entropy, manufacturing efficiency.

## I. INTRODUCTION

**R**OBOTIC manipulation of dynamic objects has broad applications in industrial manufacturing, particularly in conveyor-based assembly lines where robots handle transported products [1], [2]. Compared with the extensively studied static object manipulation problem [3], [4], dynamic object manipulation poses more challenges due to its demand for more time-efficient motion planning and stricter operational precision. Addressing these challenges is important for enhancing the efficiency and flexibility of industrial automation systems, thereby enabling more economical manufacturing.

Currently, the methods employed in real-world production lines are primarily based on classic motion planning approaches [5]. These methods require specialized designs for various scenarios, as well as complex system modeling and parameter tuning, which could be both time-consuming and labor-intensive [6]. To handle this problem, much attention has been drawn to exploring how to build an intelligent manipulation system capable of generalizing across diverse scenarios. Recent manipulation literature increasingly turns to the imitation learning paradigm [7], where expert demonstrations are collected to teach a policy to control a robot arm. In imitation learning, the generalization of a policy can be improved by scaling up the volume of demonstrations [8].

Zhuoling Li, Xiaoyang Wu, and Hengshuang Zhao are with the University of Hong Kong. Zhenhua Xu is with Tsinghua University. Corresponding author: Hengshuang Zhao (e-mail: [hszhao@cs.hku.hk](mailto:hszhao@cs.hku.hk)).

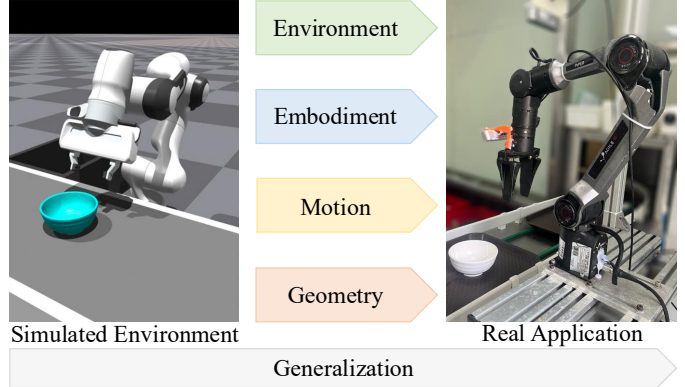


Fig. 1. Primarily using demonstrations collected from a simulator, our method can generalize across diverse environment backgrounds, robot embodiments, motion dynamics, and object geometries. Our method has been reliably deployed in a real canteen to conduct tableware collection. Without relying on any demonstration collected in this canteen, our method achieves a success rate of over 97% in seven consecutive days of operation, performing more than 10,000 tableware collection operations.

Consequently, the research community has devoted significant efforts to constructing large-scale manipulation datasets [9], [10]. However, these datasets primarily focus on static scenarios, with few public datasets addressing dynamic object manipulation. Additionally, even in static object manipulation, the generalization of the policies trained using these large-scale datasets is still limited [11], [12], implying the volume of demonstration is still far from sufficient.

Therefore, although realizing generalizable dynamic object manipulation is of huge importance, collecting demonstrations is costly and there are few public data resources [13]. Given these facts, this work studies whether strong generalization in dynamic object manipulation can be achieved without relying on numerous demonstrations. To address this question, we delve into the optimization essence of imitation learning, framing it as a distribution approximation problem. Building upon this formulation, we propose an information entropy based theoretical framework to quantify the amount of data required to achieve generalizable manipulation. From this theoretical framework, we identify two key aspects: first, reducing the complexity of redundant information in observations, and second, decreasing the ambiguity in action prediction.

According to these two key aspects, we develop a manipulation system named Generalizable Entropy-based Manipulation (GEM). GEM consists of two blocks, *i.e.*, object-centric geometry perception and hybrid action control. In object-centric geometry perception, we devise a representation that empha-

sizes the geometric structures of objects while minimizing the impact of visual appearance, thereby reducing redundant details irrelevant to manipulation. Within hybrid action control, imitation learning is combined with visual servo control to manage the moving dynamics of objects. Additionally, an efficient memory modeling strategy is proposed in the imitation learning algorithm to alleviate action prediction ambiguity.

In experiments, we implement a single GEM to support four common skills in dynamic object manipulation, *i.e.*, Pick, Put, Rotate, and Insert. Extensive experiments are conducted in both simulators and the real world to validate the effectiveness of GEM. The experiments suggest that GEM presents promising generalization across diverse environment backgrounds, robot embodiments, motion dynamics, object geometries, and in sim-to-real settings. Especially, as illustrated in Fig. 1, GEM has been successfully deployed in a real canteen to perform tableware collection. Without using demonstrations collected in this canteen, GEM achieves a 97.2% success rate over seven days of testing and more than 10,000 operations.

Summarily, the contributions of this work are as follows:

- 1) We develop an entropy-based framework to analyze the optimization of imitation learning, guiding the design of an efficient manipulation system with limited demonstrations.
- 2) We propose GEM, a system combining object-centric geometry perception and hybrid action control to achieve strong generalization in dynamic object manipulation.
- 3) We demonstrate the first real-world application of imitation learning in dynamic object manipulation, achieving over 97% success rate without in-scene demonstrations.

## II. RELATED WORKS

### A. Imitation Learning for Manipulation

Traditional robotic manipulation methods mostly rely on accurate modeling of the environment to plan action trajectories of robot arms [5]. However, manipulation often involves contact-rich interactions with objects, and accurately modeling these interactions is difficult due to the highly variable nature of contact forces [14]. Moreover, every manipulation task often requires a unique set of models and parameters, making these traditional methods difficult to generalize across different objects, environments, and robot embodiments. This necessitates substantial engineering efforts to adapt the system to new tasks or scenarios [15].

Given these limitations of traditional methods, there is a growing interest in leveraging imitation learning to address the challenges of robotic manipulation [7]. Bypassing the need for explicit system modeling and complex parameter tuning, imitation learning learns manipulation policies directly from expert demonstrations. Specifically, imitation learning trains a policy to predict expert actions based on the observations provided in demonstrations, enabling a robot to mimic expert behavior in similar scenarios. The policy is often implemented as a deep learning network [16], which can capture the complex patterns in demonstrations [17].

The two most commonly employed observation modalities in robotic manipulation are images and 3D points [5]. Correspondingly, existing imitation learning policies can be

broadly categorized into image-based [18] and point-based approaches [19]. Images are easy to obtain, and image-based policies can readily leverage large-scale public data for training [20]. However, robotic manipulation mainly concerns the geometric structures of objects, while images primarily capture the appearance of scenes, making it challenging to predict appropriate manipulation actions based solely on visual appearance. In contrast, point clouds directly represent the geometric structures of scenes, and thus they are more suitable for regressing manipulation actions [21]. Unfortunately, point cloud data is relatively scarce compared with images, resulting in a lack of promising point cloud feature extractors [22]. This limitation has historically constrained the performance of point-based manipulation policies [23]. Thankfully, some recent works about large-scale point cloud pre-training have gradually addressed this obstacle [24], [25].

### B. Data Scaling in Manipulation

The rapid progress in fields like large language models [26] suggests that increasing the quantity and diversity of training data is important for enhancing the generalization of deep learning models. Drawing on this insight, the robotic manipulation community has invested significant effort into constructing large-scale demonstration datasets [9], [10]. Leveraging these datasets, numerous studies design algorithms for training end-to-end manipulation policies, with the expectation that these policies exhibit robust generalization across diverse scenarios [11], [27]. Furthermore, some works incorporate additional types of data like object detection datasets to further enrich the knowledge base of manipulation policies [12], [28]. Nevertheless, though much resource has been invested, the generalization capabilities of the obtained policies in unseen environments are still limited.

This fact reminds us to rethink whether the data scaling paradigm inspired by large language models is directly applicable to robotic manipulation. Rather than solely focusing on constructing larger manipulation datasets or training models with more parameters, we also need to pay attention to designing an efficient manipulation paradigm that achieves economical manipulation generalization. This shift in perspective emphasizes the importance of developing methods that can leverage limited data more efficiently [29].

### C. Sim-to-Real Generalization in Manipulation

Collecting high-quality demonstration data in the real world is labor-intensive. To address this issue, many researchers have explored generating demonstrations in simulated environments [30]. These efforts aim to develop policies trained using only simulated demonstrations yet can generalize to real-world applications. A key first step towards this goal is the development of realistic simulators. Through substantial engineering efforts, several promising simulators have been built, such as MuJuCo [31], Isaac Gym [32], and Isaac Sim [33]. Leveraging these simulators, prior works have used reinforcement learning [34] or predefined kinematic procedures [35] to generate demonstrations. However, reinforcement learning often struggles to discover successful manipulation trajectories

due to its inefficient exploration [36]. Grasping objects via predefined kinematic procedures typically requires customized workflows for different scenarios, which is time-consuming. Additionally, current simulators have limited environmental diversity, restricting the variety of generated data.

Another line of works focuses on modeling the environment dynamics of manipulation tasks using classic mechanics and then employs optimization techniques to calculate actions that satisfy task constraints [14]. The observation and action pairs can then be utilized to train deep neural networks [37], [38]. This strategy effectively addresses the slow speed of optimization by distilling the action search process into a more efficient neural network [39]. Nevertheless, for complex manipulation tasks, the computation burden is too heavy to search for satisfactory actions, making it difficult to generate effective demonstrations. To tackle this problem, some works collect demonstrations in simulators through teleoperating simulated robots [40]. Although this method still requires significant human effort, it reduces hardware setup costs compared to real-world data collection.

### III. ENTROPY REDUCTION THEORETICAL FRAMEWORK

This section develops a theoretical framework by analyzing the information entropy of imitation learning, providing logical support for developing a generalizable manipulation system with only a few demonstrations.

#### A. Robotic Manipulation Problem Formulation

Robotic manipulation involves controlling a robot arm to interact with objects in the environment to achieve a specific task. The task can be defined as a sequence of actions that the robot needs to take to reach a desired goal. Therefore, the robotic manipulation problem can be conceptualized as a Markov Decision Process represented by a tuple  $\mathcal{E} = (\mathcal{S}, \mathcal{A}, \mathcal{P}, \mathcal{T}, s_0)$ . In this tuple,  $\mathcal{S}$  denotes the set including all potential states of the environment and robot.  $\mathcal{A}$  represents the actions that can be performed by the robot.  $\mathcal{P} : \mathcal{S} \times \mathcal{A} \times \mathcal{S} \rightarrow [0, 1]$  is the probability distribution governing how the current state transitions to the next state given the performed action.  $\mathcal{T}$  represents the task target set and  $s_0$  denotes the initial state.

In a specific task target  $\tau \in \mathcal{T}$  of robotic manipulation, there usually exist numerous accurate action trajectories that can lead the robot from the initial state  $s_0$  to the desired goal state  $\tau$ . We denote all the accurate trajectories as a set  $\mathcal{C}$  and each trajectory is represented as a sequence of states and actions  $\{s_0, a_0, \dots, s_{T-1}, a_{T-1}, s_T\}$ , where  $s_T = \tau$ .

To enable the robot to automatically complete the target task  $\tau$  without human intervention, researchers devise algorithms to find an optimal policy  $\pi : \mathcal{S} \rightarrow \mathcal{A}$  that maximizes the probability of reaching the target state  $\tau$  following the transition probability distribution  $\mathcal{P}$ . This objective can be expressed as learning to approximate the joint state-action distribution induced by the successful trajectories in  $\mathcal{C}$ . Specifically, let  $p_C(s_{0:T}, a_{0:T-1})$  denote the state-action sequence distribution in  $\mathcal{C}$ , the optimization objective is to minimize the Kullback-

Leibler (KL) divergence between the policy predicted distribution  $p_\pi(s_{0:T}, a_{0:T-1})$  and  $p_C(s_{0:T}, a_{0:T-1})$ :

$$\min_{\pi} D_{KL}(p_C(s_{0:T}, a_{0:T-1}) \parallel p_\pi(s_{0:T}, a_{0:T-1})), \quad (1)$$

where  $p_\pi(s_{0:T}, a_{0:T-1})$  is defined through the Markov chain:

$$p_\pi(s_{0:T}, a_{0:T-1}) = p(s_0) \prod_{t=0}^{T-1} \pi(a_t|s_t) P(s_{t+1}|s_t, a_t). \quad (2)$$

This formulation explicitly connects policy optimization with implicit distribution estimation of  $\mathcal{C}$ .

#### B. Entropy Analysis of Imitation Learning

However, in robotic manipulation, a policy  $\pi$  usually does not have access to the true state  $s_t$  at timestamp  $t$ . Its environment observation is a mapping function of  $s_t$ , written as  $o_t = f(s_t)$ . Compared with  $s_t$ ,  $o_t$  only partially reflects the environment information and may contain noise. The action to execute is sampled from  $\pi$  following  $a_t \sim \pi(o_t, \tau)$ . The policy  $\pi$  is often modeled as a deep neural network [16].

Many recent manipulation works derive  $\pi$  based on imitation learning [8], which is typically formulated as a supervised learning problem. Imitation learning requires access to a set of expert demonstrations as training data. Assume there are  $N_d$  demonstration sequences, the expert demonstration set is denoted as  $\mathcal{C}_d = \{o_t^i, \tilde{a}_t^i\}_{i=1}^{N_d}$ , where  $o_t^i$  and  $\tilde{a}_t^i$  are the observation and expert action at timestamp  $t$  of the  $i$ th demonstration. The core idea of imitation learning is employing  $\mathcal{C}_d$  as a surrogate of  $\mathcal{C}$ . Thus, the objective of imitation learning can be expressed as maximizing the likelihood of expert demonstrations under the policy-induced distribution:

$$\max_{\pi} \mathbb{E}_{(o_t^i, \tilde{a}_t^i) \sim \mathcal{C}_d} [\log \pi(\tilde{a}_t^i | o_t^i, \tau)]. \quad (3)$$

This objective can be understood as that  $\pi$  is trained to capture the joint observation-action probability distribution in  $\mathcal{C}_d$ .

In practical implementations of imitation learning, the objective in Eq. (3) is often transformed into a behavior cloning objective, which is to explicitly minimize the difference between the predicted actions and the expert actions, written as:

$$\pi^* = \arg \min_{\pi} \sum_{i=1}^{N_d} \sum_{t=0}^T L(\pi(o_t^i, \tau), \tilde{a}_t^i), \quad (4)$$

where  $L$  represents the difference measurement function, and  $\pi^*$  is the obtained optimal policy. Inspired by the recent breakthroughs in research fields like large language models [26] and image generation [41], it is believed that the distribution of  $\mathcal{C}$  can be precisely approximated by scaling up the volume of expert demonstration data  $\mathcal{C}_d$  [9], [11].

Nevertheless, collecting diverse demonstrations is expensive in robotic manipulation [42]. Although huge efforts have been invested in building large-scale manipulation datasets [9], [10], the available quantity of demonstrations is far from sufficient compared with fields like large language models [43]. Currently, the policies trained on these datasets only serve as pre-trained network weights, still requiring task-specific fine-tuning for each downstream application [27], [42].

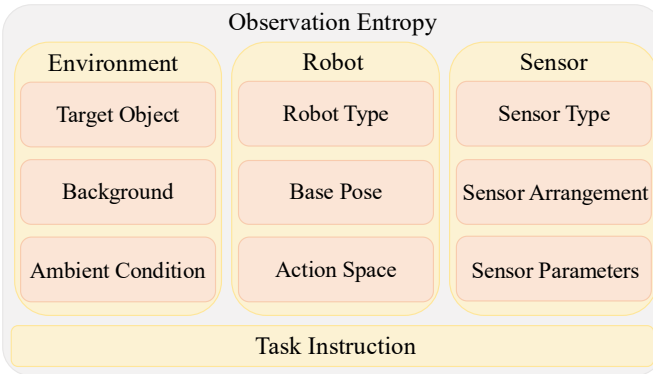


Fig. 2. This figure illustrates the primary factors affecting the observation entropy  $\mathcal{H}(\mathcal{O}_C)$ . The factors include environment, robot, sensor, and task instruction. These factors can be further divided.

Thus, exploring strategies to reduce the demonstration data requirement of imitation learning is important.

To conduct this exploration, we first specify that the optimization objective of imitation learning is to approximate the joint observation-action distribution  $p_C(o_{0:T}, a_{0:T-1})$ , which describes how to achieve successful manipulation. For notational convenience, we represent the sets of observations and actions in  $\mathcal{C}$  as  $\mathcal{O}_C$  and  $\mathcal{A}_C$ . To explore how to reduce the demonstration demand while maintaining policy performance, we need a theoretical framework to quantify the data requirement for approximating  $p_C(o_{0:T}, a_{0:T-1})$ . In information theory, the entropy  $\mathcal{H}(\mathcal{O}_C, \mathcal{A}_C)$  serves as a measure of the amount of information contained within a distribution, reflecting the inherent uncertainty or complexity of data [44]. A higher entropy indicates the distribution contains more information and requires more demonstrations to accurately approximate.

Furthermore, we decompose  $\mathcal{H}(\mathcal{O}_C, \mathcal{A}_C)$  via the chain rule:

$$\mathcal{H}(\mathcal{O}_C, \mathcal{A}_C) = \mathcal{H}(\mathcal{O}_C) + \mathcal{H}(\mathcal{A}_C|\mathcal{O}_C). \quad (5)$$

This decomposition reveals that the information entropy of imitation learning consists of two parts, the observation complexity  $\mathcal{H}(\mathcal{O}_C)$  and the action prediction ambiguity  $\mathcal{H}(\mathcal{A}_C|\mathcal{O}_C)$ . By reducing  $\mathcal{H}(\mathcal{O}_C)$  and  $\mathcal{H}(\mathcal{A}_C|\mathcal{O}_C)$ , the demonstration volume requirement can be alleviated.

In addition, we expect the manipulation performance not to compromise after reducing  $\mathcal{H}(\mathcal{O}_C)$  and  $\mathcal{H}(\mathcal{A}_C|\mathcal{O}_C)$ . To figure out how to realize this goal, it should be first noted that although there are numerous manipulation trajectories meeting constraints,  $\pi$  only needs to predict one of them to complete the task. Therefore, when reducing the entropy, the probability of selecting a suitable action leading to successful manipulation should not be decreased. To ensure this, (i) When lessening the observation complexity  $\mathcal{H}(\mathcal{O}_C)$ , we only remove redundant observation information irrelevant to inferring accurate actions. (ii) During reducing the action prediction ambiguity  $\mathcal{H}(\mathcal{A}_C|\mathcal{O}_C)$ , the policy should increase the likelihood of predicting a successful trajectory.

### C. Observation Complexity Reduction

To alleviate the demonstration data demand, we first study how to reduce the observation entropy  $\mathcal{H}(\mathcal{O}_C)$ , which mea-

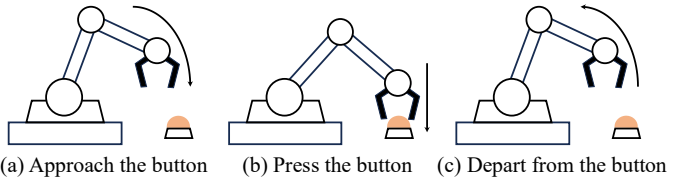


Fig. 3. The sub-figure (a)-(c) illustrate the procedures that a robot hand presses a button. We can find that if the policy input does not include historical memory and moving velocity, the policy observations are the same between sub-figure (a) and (c), in which the robot hand is approaching the button and moving away from the button, respectively.

sures the complexity of the observation set in  $\mathcal{C}$ . Specifically, we expect to reduce the redundant information in observations that is irrelevant to inferring actions, because removing such information does not hurt action prediction precision. Notably, which kinds of information are irrelevant to actions are not deterministic. They are influenced by how the manipulation system is designed. For instance, if a policy  $\pi$  directly predicts the robot hand end-effector movement and then utilizes this movement to control joint rotations based on inverse kinematics, the joint angle observation is unnecessary for inferring actions when the end-effector position observation has been provided. Therefore, the key to reducing  $\mathcal{H}(\mathcal{O}_C)$  is devising a manipulation system making most factors irrelevant to inferring actions. Then, these irrelevant factors can be excluded from observations, thereby reducing  $\mathcal{H}(\mathcal{O}_C)$ .

To more thoroughly analyze this problem, we need to know  $\mathcal{H}(\mathcal{O}_C)$  is determined by which factors. We illustrate the primary factors in Fig. 2. These main factors contributing to  $\mathcal{H}(\mathcal{O}_C)$  can be categorized into four classes, *i.e.*, environment information, robot proprioception, sensor configuration, and task instruction. Among them, the environment information includes the target object to manipulate, scene background, and ambient conditions (such as lighting brightness and air humidity). These pieces of information can be further divided, like the target object information can be classified into its physical geometry and visual appearance.

Differently, robot proprioception mainly describes the type of robot employed (like Franka Panda or UR5e), where the robot is located in the environment, and the action space (like end-effector control or joint control). Sensor configuration specifies what kinds of sensors are adopted (like RGB camera and depth sensor), how the sensors are deployed in the environment (the number of sensors and their poses), and the parameters of these sensors. A task instruction specifies the task target. It can be represented in different modalities, including text [11], image [40], voice [45], etc.

Summarily, the above four classes of factors play distinct roles in shaping the complexity of the observation set  $\mathcal{O}_C$ . To reduce  $\mathcal{H}(\mathcal{O}_C)$ , we need to design a system making most factors irrelevant to predicting actions. We explain how such a specific system is devised in Section IV.

### D. Action Prediction Ambiguity Reduction

In this subsection, we discuss how to reduce  $\mathcal{H}(\mathcal{A}_C|\mathcal{O}_C)$  in Eq. (5), which represents the action prediction ambiguity

given observations. This ambiguity is mainly caused by the multimodal nature of robotic manipulation, meaning there exist multiple valid action trajectories given the same observation [46]. For example, in the task of grasping a block, a robot arm can complete the task by approaching the block from either the left or the right side. Moreover, the ambiguity becomes more pronounced when the observation information is insufficient. For instance, Fig. 3 illustrates an example that a robot hand is pressing a button. In Fig. 3 (a)-(c), the robot hand is approaching the button, pressing the button, and departing from the button, respectively. If the policy input only includes the current visual observation and robot joint angles, the observations are the same between Fig. 3 (a) and (c), while the accurate end-effector moving directions are different.

Hence, larger action prediction ambiguity not only increases demonstration demand, but also raises the risk of making incorrect decisions. To handle this problem, more comprehensive information supporting accurate action prediction should be provided. According to the example in Fig. 3, incorporating historical memory into policy observation is effective, especially for complex and long-chained manipulation tasks. This is because historical memory enables the policy to know which manipulation steps have been completed.

However, previous works often find incorporating historical memory degrades success rates [8]. One key reason is that these works choose to model memory using historical action trajectories. As analyzed in VIP [40], when the attribute to predict (the future action trajectory in this case) and a part of the policy input (the historical action trajectory) fall in the same modality, the policy often chooses to overlook the input information in other modalities (like images). This is because it is easier to predict future actions based on historical actions than information in different modalities. A learnable network tends to choose the easiest way of regressing future actions while overlooking the exploitation of information in other modalities. This problem is termed as shortcut learning and has been well analyzed in previous literature [47].

An effective strategy for handling the shortcut learning problem is preventing using input in the same modality as output. In this case, it means avoiding modeling memory with historical action trajectories. Drawing on this insight, we represent memory with images. However, directly incorporating historical images into policy input leads to a huge computational burden [48]. To address this problem, we develop an efficient recurrent encoder for modeling visual memory [49], which is explained in Section IV-E. By utilizing historical memory,  $\mathcal{H}(\mathcal{A}_C | \mathcal{O}_C)$  is reduced significantly.

#### E. Multimodal Distribution Estimation

As described in Section III-B, imitation learning optimizes a policy  $\pi$  to capture the probability distribution inherent in demonstration data. Due to the action prediction ambiguity, the expert demonstration distribution is multimodal. Therefore,  $\pi$  should be capable of fitting a multimodal distribution.

Recently developed policies mostly regress future actions directly, and the policy network parameters are updated based on loss functions like mean absolute error [8]. Such loss

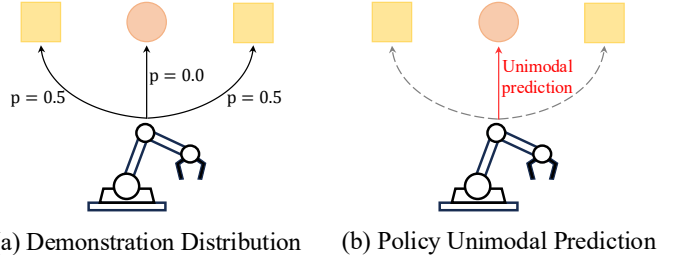


Fig. 4. As shown in the sub-figure (a), in the task “pick up a yellow square”, the accurate actions present a multimodal distribution due to the existence of two yellow squares. In the sub-figure (b), if the policy is an unimodal distribution estimator, the action corresponding to the minimum expected error is towards the pink circle, an incorrect moving direction.

function designs imply these policies regress to unimodal distributions with fixed uncertainties [50]. In other words, these policies are unimodal distribution estimators. In Fig. 4, we show what happens when we employ an unimodal distribution estimator to fit a multimodal distribution. Specifically, the robot needs to pick up a yellow square, and the valid actions present a multimodal distribution due to the existence of two yellow squares. The optimization objective is to minimize the regression error between the multimodal demonstration distribution and unimodal policy prediction, which is formulated in Eq. (4). Similar to the process of mean regression [51], this optimization process leads to an action prediction taking the mean of all valid actions (the mean expected value of this multimodal distribution). As visualized in Fig. 4 (b), the robot moves towards an incorrect target, the middle position between these two yellow squares.

To handle this problem, we propose to model the policy output as Gaussian Mixture Distribution [52] with  $K$  components, which can naturally represent multimodal distributions. What the policy predicts is the means, variances, and weights of these Gaussian components, denoted as  $\mu_k$ ,  $\sigma_k^2$ , and  $\alpha_k$  for the  $k$ th component, respectively. Thus,

$$\pi(a_t | o_t, \tau) = \sum_{k=1}^K \alpha_k \mathcal{N}(\mu_k, \sigma_k^2). \quad (6)$$

The component weights  $\{\alpha_k\}_{k=1}^K$  satisfy  $\sum_{k=1}^K \alpha_k = 1$  and  $\alpha_k \geq 0$  for all  $k \in \{1, 2, \dots, K\}$ . We update the policy following the optimization objective in Eq. (3). In this way, our developed policy is able to fit complex demonstration data with multimodal distributions.

Summarily, the content in this subsection ensures that we can approximate the multimodal demonstration distribution  $p_C(o_{0:T}, a_{0:T-1})$  accurately, and the analysis from Section III-B to Section III-D enables a policy to learn  $p_C(o_{0:T}, a_{0:T-1})$  with fewer demonstrations. Guided by these insights, we develop a generalizable manipulation system GEM, which is elaborated in Section IV.

## IV. GENERALIZABLE ENTROPY-BASED MANIPULATION

In this section, we introduce our developed dynamic object manipulation system GEM. GEM is devised following the

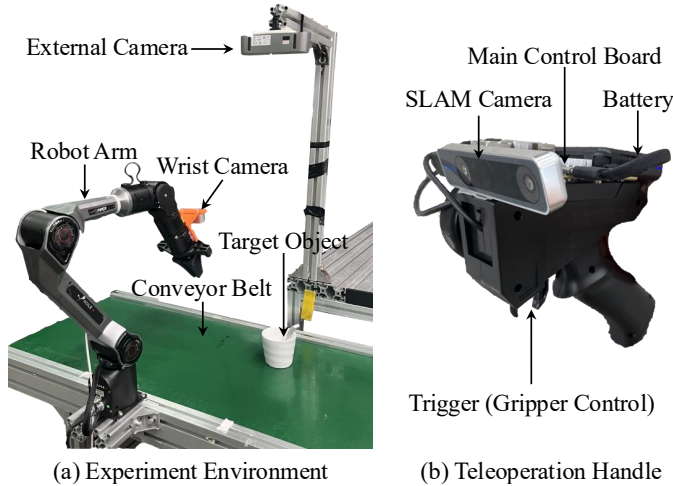


Fig. 5. Our built hardware platform and remote teleoperation handle. Specifically, Sub-figure (a) illustrates the real robot environment for studying dynamic object manipulation. GEM controls the robot arm to perform diverse tasks given the observations from the external and wrist RGB-D cameras. Sub-figure (b) shows our designed remote handle for teleoperating the robot arm to collect demonstration data.

theoretical framework in Section III. Only using hundreds of manual demonstrations and thousands of programmatic demonstrations collected from simulated environments, GEM can generalize to diverse unseen target objects, moving dynamics, background environments, and robot embodiments.

#### A. Hardware Setup

To study the dynamic object manipulation problem, we build a hardware platform as shown in Fig. 5. In this platform, objects are driven by a conveyor belt at an adjustable velocity. A robot arm with a gripper is mounted on a side of this conveyor belt to manipulate the target object. Two RGB-D cameras are deployed to capture environment observations, one on the robot arm (the wrist camera) and the other on a fixed third-person perspective bracket (the external camera). GEM controls the robot arm to manipulate objects based on the observations from these two cameras.

As illustrated in Fig. 5 (b), a teleoperation handle is designed to teleoperate the robot arm in Fig. 5 (a). Specifically, we control the motion of the robot arm end-effector based on the relative pose change of the handle derived from the SLAM camera. The opening and closing of the gripper is regulated through the trigger pull degree. A battery is mounted on the handle to power all the devices in this handle. The control signals from the SLAM camera and trigger are wirelessly transmitted to the robot arm by the main control board, thereby enabling flexible remote teleoperation. The teleoperation handle is only utilized to collect demonstration data for training the learnable network, which we explain in Section IV-E. The handle is not used when testing the method.

#### B. GEM Overall Framework

The overall framework of GEM is illustrated in Fig. 6. It can be observed that GEM comprises two blocks, *i.e.*, object-centric geometry perception and hybrid action control. The

object-centric geometry perception block extracts 3D point clouds of the target objects in the external and wrist sensor views. The design of this block follows the principles summarized in Section III-C, which points out the importance of excluding factors irrelevant to predicting actions from observations. In this way, the observation entropy  $\mathcal{H}(\mathcal{O}_C)$  is decreased and less data is required to achieve strong generalization.

In hybrid action control, we combine a classic visual servo control algorithm [1] and an imitation learning based neural network control algorithm to compute the robot end-effector trajectories. Specifically, the visual servo control algorithm is responsible for tracking the target object to manipulate, and the neural network control algorithm (the recurrent probabilistic network) generates manipulation actions of different skills according to input skill type instructions. The robot end-effector action is the sum of the actions produced by these two algorithms. This design allows the recurrent probabilistic network not need to consider the moving dynamics (like velocity and acceleration) of the target object, further reducing  $\mathcal{H}(\mathcal{O}_C)$ . In addition, the developed recurrent probabilistic network can model long-term historical memory, thereby decreasing the action prediction entropy  $\mathcal{H}(\mathcal{A}_C|\mathcal{O}_C)$ . The output actions of the recurrent probabilistic network are represented in Gaussian Mixture Distributions as described in Section III-E. Hence, the manipulation multimodal ambiguity problem is addressed.

To enable GEM to adapt to different robot hand embodiments, the hybrid action control block predicts the translation and orientation of the robot end-effector. Based on this prediction, we calculate the corresponding robot joint rotations via inverse kinematics [53], and these rotations are utilized to operate the movements of robot arms. This strategy allows for compatibility with various robot embodiments.

#### C. Object-Centric Geometry Perception

This subsection describes a perception module that produces observations with low  $\mathcal{H}(\mathcal{O}_C)$ . To design this module, we first identify the redundant factors in observations. If these factors do not provide necessary information for predicting actions, we can exclude them from observations to reduce  $\mathcal{H}(\mathcal{O}_C)$  while maintaining manipulation performance. Fig. 2 summarizes the primary factors affecting  $\mathcal{H}(\mathcal{O}_C)$ . By analyzing them, we first observe that successful manipulation mainly depends on the geometric structures of objects rather than their appearances. However, most embodied networks take images as input [46], which conveys visual appearance directly but lacks explicit 3D geometry. To handle the missing geometry, we employ uncolored 3D points as policy input. These 3D points can be easily accessed via the RGB-D cameras shown in Fig. 5. Besides, some recent deep learning models can produce promising dense depth maps from monocular or binocular images [54], [55], which facilitates obtaining depth. In addition, 3D points provide representation less affected by sensor parameters. This is because 3D points exist in the real world and are not represented in the pixel coordinate system.

Since environment background does not affect manipulation interaction, we adopt a lightweight instance segmentation model [56] to segment points of concerned objects and remove

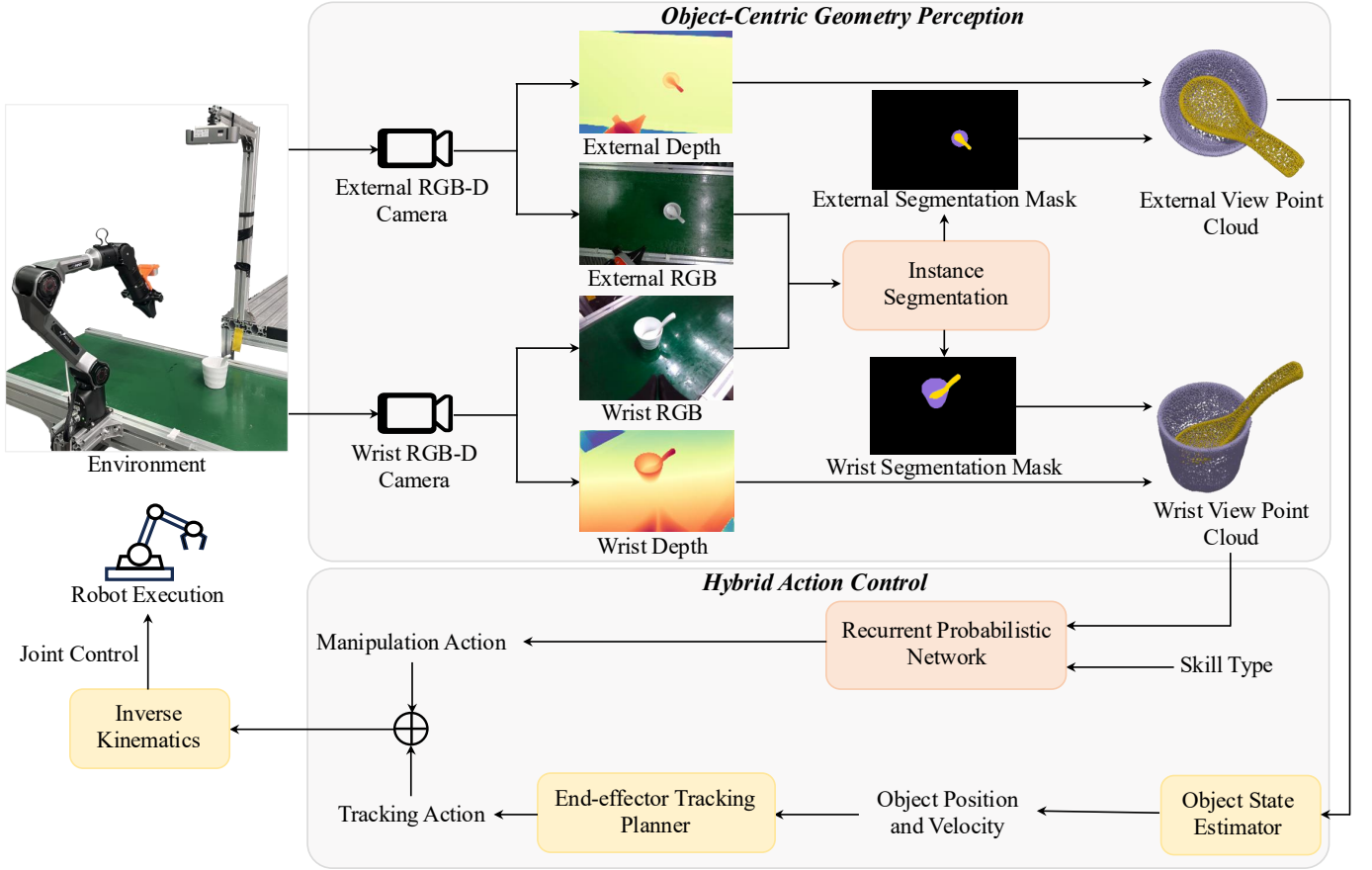


Fig. 6. The overall pipeline of GEM. GEM primarily consists of two blocks, the object-centric geometry observation and hybrid action control. In object-centric geometry observation, we exclude the many factors irrelevant to predicting actions from policy observation, and thus the observation entropy is reduced. In hybrid action control, we combine classic visual servo control with learnable network control. In the learnable network control, we design the recurrent probabilistic network, which models historical vision observations as memory. In this way, the action prediction entropy is decreased. Only using hundreds of demonstrations for training, GEM can be generalized to diverse unseen scenes. In this figure, the pink modules are implemented based on learnable neural networks and the yellow modules are non-learnable algorithms.

background points. Such an instance segmentation model is readily obtainable due to the availability of many open-world segmentation models [57]. Notably, multiple objects could be observed in a single frame. For example, in the “pick up the spoon out of the cup” task illustrated in Fig. 6, the 3D points of both the spoon and cup are important. In industrial applications, as manipulation procedures are predetermined, we can define which objects to segment in advance. For tasks with unfixed procedures, large language models [26] could be employed to reason about which objects to focus on.

Notably, a manipulation policy needs to classify the points belonging to different objects, like the cup and spoon in the example shown in Fig. 6. Nevertheless, using uncolored 3D points as policy input makes this classification challenging. To address this obstacle, we leverage instance segmentation results to append distinct instance identifiers (IDs) to the points of various objects. With the instance IDs, the object classification problem is addressed. Summarily, combining the above designs, we propose to use uncolored 3D points of concerned objects appended with corresponding instance IDs as the observation representation with low  $\mathcal{H}(\mathcal{O}_c)$ .

#### D. Hybrid Action Control

This subsection explains how to further reduce  $\mathcal{H}(\mathcal{O}_c)$  by devising the hybrid action control block in Fig. 6. The basic idea is to leverage the complementary strengths of classic control and learnable network control. Classic control algorithms, such as visual servo control [1], excel at stably and rapidly guiding the robot arm to approach and track moving objects. However, they often struggle with collision-rich interactions, such as grasping, inserting, and rotating objects. This is because of the complexity of modeling contact dynamics. On the other hand, learnable network control methods, particularly those grounded in imitation learning, are adept at handling such interactions by capturing the underlying patterns in expert demonstrations. By combining these two approaches, we enable the learnable network to concentrate on generating collision-rich interactions, thereby reducing  $\mathcal{H}(\mathcal{O}_c)$ .

As described in Section IV-C, the object-centric geometry perception module extracts the 3D points of the target object to manipulate from both the external and wrist sensors. Denote the two groups of 3D points as  $\{(x_i^e, y_i^e, z_i^e)\}_{i=1}^{N^e}$  and  $\{(x_i^w, y_i^w, z_i^w)\}_{i=1}^{N^w}$ , respectively. The classic control, consisting of an object state estimator and an end-effector tracking

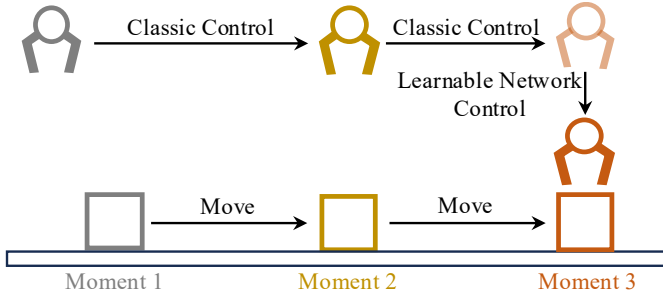


Fig. 7. This figure illustrates how classic control and learnable network control are combined. Specifically, classic control is utilized to approach and track the moving target object. The learnable network control starts generating manipulation actions once stable tracking is achieved. The grippers and target objects marked in gray, dark yellow, and reddish brown correspond to their positions at Moments 1, 2, and 3, respectively. The pink gripper indicates the position that would be achieved using classic control alone at Moment 3.

planner as shown in Fig. 6, operates the robot hand to track the moving target object based on the external view 3D points. Specifically, the object state estimator first computes the top centroid of the external view 3D points, denoted as  $(x_c^e, y_c^e, z_c^e)$ , where  $x_c^e = \frac{1}{N_e} \sum_{i=1}^{N_e} x_i^e$ ,  $y_c^e = \frac{1}{N_e} \sum_{i=1}^{N_e} y_i^e$ , and  $z_c^e = \max_{i=1}^{N_e} z_i^e$  (the positive z-axis points upward). Based on the top centroids at different timestamps, we can estimate the target object velocity  $(v_x, v_y, v_z)$  using Gaussian process regression [58] implemented in the object state estimator. If the target object is occluded in the external view camera, its real-time top centroid is also predicted by this estimator based on historical centroid records using Gaussian process regression.

The control target of the end-effector tracking planner is to make the end-effector stably track the motion of the target object. In other words, the relative position offset between the end-effector and the target object should be maintained at the preset distances  $(x^p, y^p, z^p)$ . In addition, to ensure the wrist RGB-D camera can clearly view the target object, the orientation of the end-effector should be kept at the preset Euler angles  $(\theta_x^p, \theta_y^p, \theta_z^p)$ . Summarily, the tracking action generated by the end-effector tracking planner comprises three parts, the tracking position  $(x_c^e + x^p, y_c^e + y^p, z_c^e + z^p)$ , tracking orientation  $(\theta_x^p, \theta_y^p, \theta_z^p)$ , and tracking velocity  $(v_x, v_y, v_z)$ .

Based on the tracking action, the end-effector first approaches the target object, as visualized in Moment 1 of Fig. 7. Then, at Moment 2, the end-effector achieves a stable tracking status. In this status, the moving target object appears stationary in the view of the wrist camera. After attaining this status, the learnable network (the recurrent probabilistic network) starts to predict manipulation actions for collision-rich interactions with the target object, as shown in Moment 3. Since the network generates manipulation actions based on the wrist-view 3D points  $\{(x_i^w, y_i^w, z_i^w)\}_{i=1}^{N^w}$ , the original dynamic object manipulation problem is transformed into a static object manipulation problem in the view of the network. Hence, the motion pattern of the target object is excluded from the factors affecting observations, meaning  $\mathcal{H}(\mathcal{O}_c)$  is reduced. Besides, this design fixes the relative position between the end-effector and the target object in the beginning of manipulation action

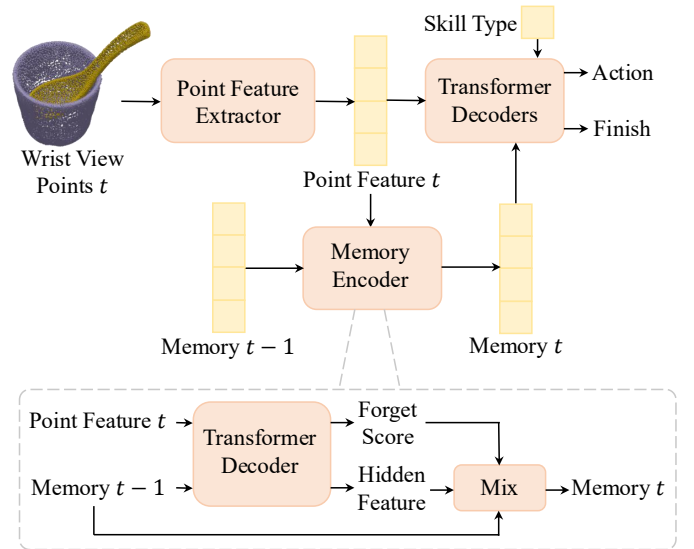


Fig. 8. The overall framework of the proposed recurrent probabilistic network, which takes the 3D points of concerned objects as input and includes a memory encoder to manage the historical observation memory.

generation as  $(x^p, y^p, z^p)$ , which further decreases  $\mathcal{H}(\mathcal{O}_c)$ .

The manipulation action predicted by the network includes the position offset  $(x^w, y^w, z^w)$  and orientation offset  $(\theta_x^w, \theta_y^w, \theta_z^w)$ . The end-effector control target output by the hybrid action control block is the sum of the tracking action and manipulation action. Therefore, the end-effector control target consists of the position target  $(x_c^e + x^p + x^w, y_c^e + y^p + y^w, z_c^e + z^p + z^w)$ , orientation target  $(\theta_x^p + \theta_x^w, \theta_y^p + \theta_y^w, \theta_z^p + \theta_z^w)$ , and velocity target  $(v_x, v_y, v_z)$ . Afterwards, the end-effector control target is converted into robot joint rotations based on inverse kinematics. This design enables a single GEM system to be applied to different robot embodiments.

### E. Recurrent Probabilistic Network

Section IV-D has described how classic control and learnable network control are combined in the hybrid motion control block. This part further elaborates the structure details of the recurrent probabilistic network used in learnable network control. The overall framework of this network is illustrated in Fig. 8. To concentrate on the geometry of objects rather than appearance, the recurrent probabilistic network takes the wrist view 3D points produced by the object-centric geometry perception block as the main input. For the 3D points perceived at timestamp  $t$ , it first employs a point feature extractor to encode the 3D points into semantic-rich feature tokens  $F_t \in \mathbb{R}^{l_p \times c}$ , where  $l_p$  denotes the token number and  $c$  is the token length. In this work, we model the point feature extractor with Sonata [25], a recent promising point network. However, the input of Sonata should be colored points, while ours are uncolored points appended with instance IDs. To bridge this gap, we feed the instance IDs into Sonata as surrogate color information. Therefore, the points of various object instances in Fig. 8 are visualized with different colors.

The memory encoder shown in Fig. 8 is to fuse  $F_t$  and the memory feature at timestamp  $t-1$ , denoted as  $M_{t-1} \in \mathbb{R}^{l_m \times c}$ ,

into the new memory feature  $M_t \in \mathbb{R}^{l_m \times c}$ . To this end, the memory encoder first employs a Transformer decoder [59] to conduct feature interaction between  $M_{t-1}$  and  $F_t$ . Specifically,  $M_{t-1}$  is used as the query embedding, and  $F_t$  is the key and value embeddings. The feature output by this Transformer decoder is transformed into the forget score  $G_t \in \mathbb{R}^{l_m \times 1}$  and hidden feature  $H_t \in \mathbb{R}^{l_m \times c}$  by two multilayer perceptron layers (MLPs). Afterwards, in the Mix module visualized in Fig. 8,  $M_t$  is calculated following:

$$M_t = \sigma(G_t) \odot H_t + (1 - \sigma(G_t)) \odot M_{t-1}, \quad (7)$$

where  $\sigma(\cdot)$  represents the Sigmoid function. At the beginning of manipulation, the memory feature is initialized as a zero embedding. Taking these designs, the historical memory is updated in an auto-regressive style, and  $\mathcal{H}(\mathcal{A}_C | \mathcal{O}_C)$  is decreased.

Then,  $M_t$ ,  $F_t$ , and a skill type embedding  $S_t \in \mathbb{R}^{1 \times c}$  are concatenated and input to three Transformer decoders.  $S_t$  is a learnable token specifying which skill to perform, and the supported skills include Pick, Place, Rotate, and Insert. The feature interaction process in decoders is similar to the implementation in ACT [8], where a chunk of  $N_a$  action tokens is utilized to conduct feature interaction with the input feature. Then, the action tokens are decoded as the action probability distributions of future  $N_a$  timestamps and a binary finish flag. As described in Section III-E, the action probability distributions are represented as the means, variances, and component weights of Gaussian mixture distribution. The finish flag indicates whether the execution of the manipulation skill has been completed. If completed, the network stops generating actions until the next time of performing a skill. In training, the network is updated following Eq. (3) as described in Section III-E. During testing, the action with the maximum probability is selected for execution.

#### F. Efficient Demonstration Collection

Combining the aforementioned techniques, we derive a low-entropy manipulation system, which exhibits stronger generalization with less demonstration data. In this part, we introduce how the demonstration data is efficiently collected to support various manipulation skills within a single system.

Demonstration data can be collected in both simulated environments and the real world. Data collection in simulated environments is usually more efficient, but the visual fidelity of existing simulators is still limited. This limitation restricts existing simulated data generation. Thankfully, our network takes uncolored 3D points as input, avoiding the visual fidelity problem. Therefore, our method can generalize to real-world applications even though only using simulated data.

Nevertheless, there is no public simulated environment for dynamic object manipulation. To bridge this gap, we build the first such environment based on Isaac Gym [32]. As shown in Fig. 9 (a), the environment layout is similar to the real platform in Fig. 5. As mentioned in Section IV-C, geometric structure information of objects is essential for successful manipulation. To enable our method to generalize to objects in diverse geometries, we gather 3D assets of 30 representative geometric structures from the GSO dataset [60] to produce demonstration data. These 3D assets are visualized in Fig. 9 (b).

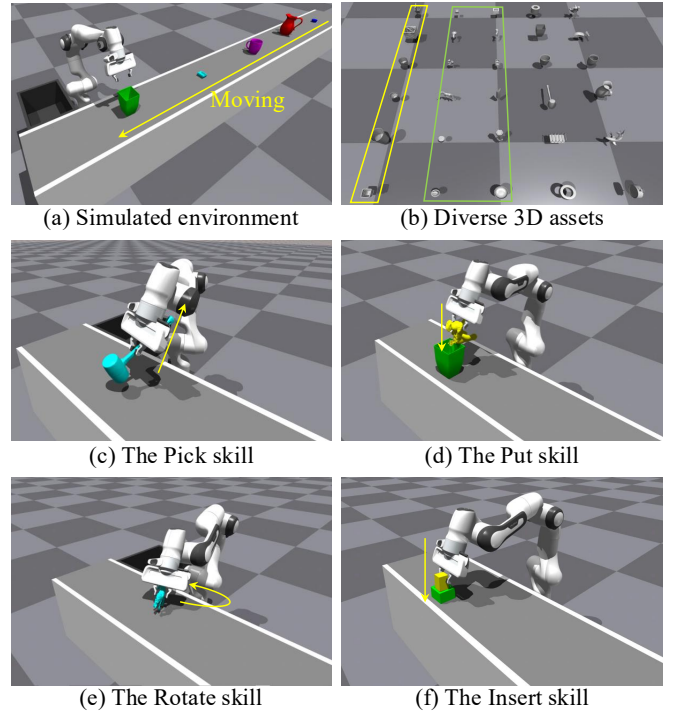


Fig. 9. This figure illustrates our simulated dynamic object manipulation environment. (a) An overview of the environment, where diverse objects are moving on a conveyor belt. (b) We collect 3D assets in 30 representative geometric structures to collect demonstrations. (c) The Pick skill. (d) The Put skill. (e) The Rotate skill. (f) The Insert skill.

This work supports the four common skills including Pick, Place, Rotate, and Insert. These four skills are shown in Fig. 9 (c)-(f), respectively. Specifically, Pick requires the robot to pick up the moving object from the conveyor belt. Place needs the robot to put an object into a moving container on the conveyor belt. Rotate demands the robot to rotate the moving object to a target orientation. The target orientation in this work is prompted to the network by providing a reference observation, which is the point cloud of the manipulated object in the goal 3D orientation from the perspective of the network. Insert involves inserting an object into a container with a precisely sized opening, ensuring the object is aligned at the specified pose. The Insert task illustrated in Fig. 9 (f) only allows two millimeters of position error.

During gathering demonstrations, all the 30 assets can be used to collect Pick data. For Put, the 12 small-sized assets highlighted by a green box in Fig. 9 (b) are put into the 5 huge-sized containers marked by a yellow box. In Rotate, the 6 assets lacking rotational symmetry are utilized to collect data. For Insert, due to the size matching requirement between the insert object and the container, we only utilize the assets shown in Fig. 9 (f). Notably, the 3D assets are colored with random pure colors instead of being rendered with more realistic appearances. This is because our method takes uncolored point clouds as input, so there is no need to spend computational resources on rendering appearances.

Among these four skills, Pick requires human knowledge to decide reasonable grasp positions. For example, in Fig. 9 (c), the robot should grasp the hammer handle rather than the

hammer head. Due to this requirement, the Pick data should be collected through human teleoperation. Specifically, we use our designed teleoperation handle shown in Fig. 5 (b) to collect 20 demonstrations for every 3D asset. In this way, 600 Pick demonstrations are obtained. Different from Pick, the demonstration data of the other three skills can be generated automatically through preprogrammed manipulation procedures. This is because we have the true state information of all objects in simulated environments. Hence, we build an automatic pipeline to generate data for these three skills without human intervention. A total of 2000 demonstrations are derived for each of these three skills.

## V. EXPERIMENTAL VERIFICATIONS

### A. Experimental Settings

1) *Implementation Details*: We train the recurrent probabilistic network using the 6,600 demonstrations collected in Section IV-F for 10K optimization iterations. The training takes about 14 hours on a single RTX4090 GPU. The optimizer is AdamW [61] and the learning rate is  $1e - 4$ . The training batch size is 32. The image resolutions of the two RGB-D cameras are both  $640 \times 480$ . The action chunk size  $N_a$ , memory token number  $l_m$ , and feature channel number  $c$  are set to 20, 200, and 512, respectively. GEM controls the robot at a frequency of 20 HZ.

2) *Testing Protocols*: We test GEM in both the simulated environment in Fig. 9 and the real platform in Fig. 5. The primary evaluation metric is the task completion success rate. In Pick, the objects in various geometric structures are successively conveyed on the conveyor belt. The success condition for Pick is the gripper successfully picks the moving object up. In Put and Insert, an object and a container are moving on a conveyor belt. Success is defined as the robot arm placing the object inside the container. For Rotate, the robot hand grasps and rotates the object on the conveyor belt to the target orientation. Success is achieved if the yaw, pitch, and roll errors are all within 5 degrees. The default moving speed of the conveyor belt is 0.1 m/s. To mitigate the influence of random errors, we conduct each experiment for 100 times to compute the average success rate.

### B. Method Comparison

This subsection compares GEM with previous manipulation methods in dynamic object manipulation. Although the classic kinematics-based methods can also handle dynamic object manipulation after precise system identification and careful parameter tuning, they demand special algorithm designs for different tasks and testing environments. This task-dependent characteristic violates the focus of this work, how to improve the generalization of a manipulation system. Therefore, we mainly compare GEM with the recent learning-based methods, which present better generalization.

The compared methods include AnyGrasp [37], ConvMLP [62], RVT-2 [63], ACT [8], Diffusion Policy (DP) [46], OpenVLA [11], and PI0 [12]. Among them, AnyGrasp can generate grasp pose candidates based on the 3D points of the target object. Then, the robot arm selects the grasp pose

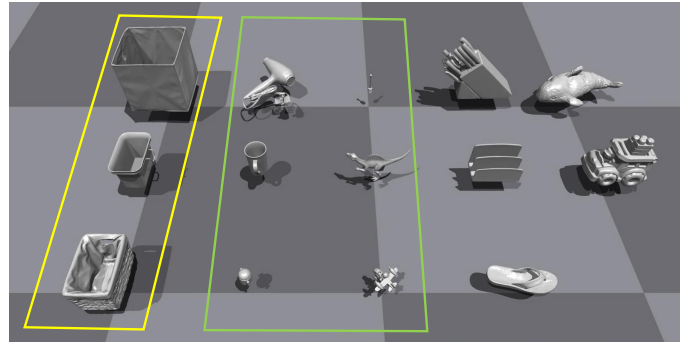


Fig. 10. This figure illustrates the 14 selected objects in diverse geometric structures for out-of-domain manipulation evaluation. All the assets are used for Pick. In Put, the small-sized assets highlighted in a green box are required to be put in the containers marked in yellow. The ten 3D assets lack of rotational symmetry are employed in Rotate.

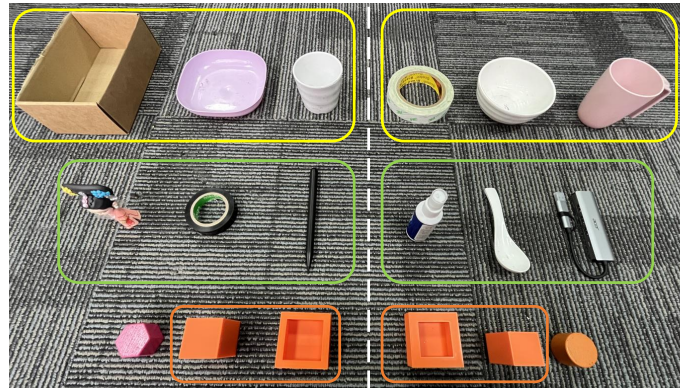


Fig. 11. The 18 objects in diverse geometries that are used to conduct the real-world manipulation experiments. The left 9 objects can be used for collect demonstrations and are used in in-domain evaluation. The right 9 objects are for out-of-domain validation. All the objects can be used in Pick. For Put, one of the small-sized objects highlighted in the green box is put in one of the containers marked in the yellow box. The USB adapter and spoon are employed in Rotate. The objects in the orange box are for Insert, which also only allows two millimeters of manipulation error.

with the highest confidence and grasps the target based on kinematic control. Since AnyGrasp only predicts the grasp pose of each object for once, the grasp is executed in an open-loop manner. RVT-2 is a representative two-stage method that takes RGB-D information as input and processes this information based on point cloud reconstruction. The inputs of the other compared methods are the wrist and external view images. Among them, ConvMLP, ACT, and DP are lightweight neural networks based on image observations. OpenVLA and PI0 are two influential vision-language-action (VLA) models. As OpenVLA and PI0 contain billions of parameters, their inference speeds are limited.

1) *Simulated Comparison*: This part compares GEM with the aforementioned counterparts in the simulation tasks described in Section V-A. Since AnyGrasp is for generating grasp poses, we only test it in Pick tasks. The algorithms in the hybrid action control module are utilized to help AnyGrasp handle the moving dynamics of objects. The other compared methods are trained using the same demonstrations as our recurrent probabilistic network. Because the compared models

TABLE I  
SUCCESS RATE AND SPEED COMPARISON WITH PREVIOUS METHODS IN SIMULATION.

Method	Pick $\uparrow$	Put $\uparrow$	Rotate $\uparrow$	Insert $\uparrow$	Avg_in $\uparrow$	Pick_o $\uparrow$	Put_o $\uparrow$	Rotate_o $\uparrow$	Insert_o $\uparrow$	Avg_out $\uparrow$	Avg $\uparrow$	Speed (HZ) $\uparrow$
AnyGrasp	0.41	-	-	-	-	0.43	-	-	-	-	-	4.35
ConvMLP	0.06	0.19	0.05	0.00	0.08	0.00	0.08	0.00	0.00	0.02	0.05	17.54
ConvMLP*	0.28	0.48	0.19	0.01	0.24	0.06	0.35	0.02	0.00	0.11	0.18	13.16
RVT-2	0.08	0.24	0.03	0.00	0.09	0.00	0.14	0.00	0.00	0.04	0.07	31.48
RVT-2*	0.47	0.62	0.15	0.27	0.38	0.18	0.50	0.00	0.12	0.20	0.29	19.69
ACT	0.14	0.29	0.10	0.00	0.13	0.05	0.22	0.00	0.00	0.07	0.10	43.48
ACT*	0.62	0.75	0.53	0.44	0.59	0.26	0.65	0.08	0.27	0.32	0.46	23.70
DP	0.09	0.24	0.07	0.00	0.10	0.00	0.17	0.00	0.00	0.04	0.07	27.32
DP*	0.55	0.70	0.46	0.36	0.52	0.18	0.54	0.05	0.23	0.25	0.39	17.86
OpenVLA	0.11	0.26	0.08	0.00	0.11	0.07	0.24	0.01	0.00	0.08	0.10	1.61
OpenVLA*	0.64	0.74	0.46	0.35	0.55	0.35	0.68	0.06	0.29	0.35	0.45	1.58
PIO	0.23	0.36	0.18	0.00	0.19	0.12	0.29	0.10	0.00	0.13	0.16	1.97
PIO*	0.68	0.81	0.59	0.65	0.68	0.50	0.75	0.14	0.43	0.46	0.57	1.92
GEM (Ours)	0.88	0.98	0.83	0.80	0.87	0.77	0.91	0.70	0.72	0.78	0.83	23.81

TABLE II  
SUCCESS RATE WITH PREVIOUS METHODS IN REAL WORLD TASKS.

Method	Pick $\uparrow$	Put $\uparrow$	Rotate $\uparrow$	Insert $\uparrow$	Avg $\uparrow$
AnyGrasp	0.12	-	-	-	-
ConvMLP	0.00	0.00	0.00	0.00	0.00
ConvMLP*	0.06	0.38	0.02	0.00	0.12
RVT-2	0.02	0.15	0.00	0.00	0.04
RVT-2*	0.17	0.59	0.08	0.04	0.22
ACT	0.08	0.23	0.05	0.00	0.09
ACT*	0.53	0.76	0.40	0.35	0.51
DP	0.05	0.17	0.01	0.00	0.06
DP*	0.46	0.70	0.32	0.25	0.43
OpenVLA	0.00	0.00	0.00	0.00	0.00
OpenVLA*	0.29	0.35	0.14	0.00	0.20
PIO	0.00	0.00	0.00	0.00	0.00
PIO*	0.37	0.58	0.21	0.00	0.29
GEM (Ours)	0.92	0.96	0.79	0.74	0.85

have no designs for dynamic object manipulation, we test them in two modes, the sole mode and hybrid mode. The sole mode means the robot movement is solely controlled by a network output. In the hybrid mode, the network output is combined with visual servo tracking like our developed hybrid action control module. In this way, the original dynamic object manipulation problem is converted into a static problem, which favors the performances of the compared methods.

As mentioned in Section IV-F, we collect 30 diverse assets to generate demonstrations and train the compared methods except AnyGrasp. To verify their out-of-domain generalization on unseen geometries, we additionally select 14 new assets, as shown in Fig. 10, to conduct experiments. The out-of-domain Insert validation is conducted using blocks similar to the ones shown in Fig. 9 but we randomly change the block sizes.

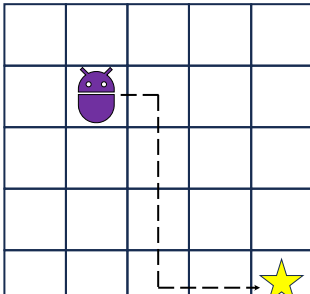
The success rates and inference speeds of all the methods are presented in Table I. Specifically, the 2<sub>nd</sub> – 6<sub>th</sub> columns are the success rates of in-domain evaluations based on the assets shown in Fig. 9 (b). The 7<sub>th</sub> – 11<sub>th</sub> columns correspond to the out-of-domain success rates of using the assets in Fig. 10. Avg<sub>in</sub>, Avg<sub>out</sub>, and Avg refer to the average success rates of in-domain tests, out-of-domain tests, and all tests, respectively. The inference speeds reported in the

13<sub>th</sub> column are the model inference frequencies tested on an RTX4090 GPU. An asterisk (\*) following the method name indicates that the method is validated in the hybrid mode. The hybrid mode increases the inference time compared to the sole mode (denoted without the asterisk) because of the additional adoption of an instance segmentation model.

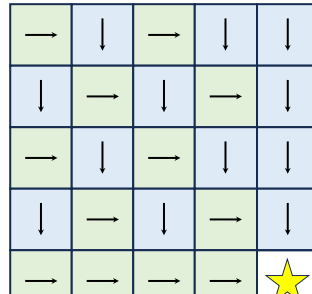
According to the results, we can find that GEM achieves the best success rates in performing all the skills. This is partly because of the efficient structure of the recurrent probabilistic network on perceiving object geometries based on points. In addition, it is observed that the methods in the hybrid mode significantly outperform the ones in the sole mode, which is attributed to that our hybrid action control module alleviates the manipulation challenge. For AnyGrasp, we find it generates promising pick poses. However, it works in an open-loop manner, which restricts its effectiveness. Though RVT-2 uses depth information like our method, its network architecture is inefficient in geometry information exploitation, resulting in its unsatisfactory success rates. Comparing the results of the VLA models and other lightweight networks like ACT, we observe VLAs generally present better out-of-domain generalization thanks to they are pre-trained on numerous data. However, the speeds of VLAs are slower. The slow inference does not affect the success rates significantly in simulated environments because the simulation is paused during model inference, but it harms performances in real tasks significantly.

2) *Real Robot Comparison*: This study compares GEM with the aforementioned counterparts in real-world tasks using the experiment platform introduced in Fig 5. The objects illustrated in Fig. 11, which are in diverse geometries and sizes, are selected to conduct this comparison. Specifically, we use the left nine objects in Fig. 11 to collect 20 demonstrations for every skill. Then, the total of 80 demonstrations are utilized to fine-tune the policies that have been trained using the simulation data. Finally, employing the same nine objects, we test their in-domain performances in the hybrid mode.

We do not compare the out-of-domain results in this experiment because we find the generalization of the compared methods is generally limited. This is because the color differences between in-domain and out-of-domain objects disturb their action prediction. In the simulation, all the objects are



(a) The MazeNav environment



(b) The expert policy

Fig. 12. Subfigure (a) illustrates the MazeNav task, where a robot is initialized in a random grid of the  $5 \times 5$  maze and needs to find a path to reach the yellow star. The yellow star is always in the bottom-right corner of the maze. Subfigure (b) visualizes the action of the expert policy in every grid.

rendered with pure colors, so the compared methods generalize successfully to some extent according to the results in Table I. Nevertheless, in real-world validation, the appearances between in-domain and out-of-domain objects are quite different. Differently, GEM can directly generalize to real world-tasks even though trained utilizing only simulated data, according to the sim-to-real results in Section V-E. This result highlights the advantage of using uncolored 3D points.

The real robot comparison result is presented in Table II, where we can find that GEM presents high success rates after tuning using only 80 demonstrations. Besides, the results of the compared methods in the hybrid mode significantly outperform the results in the sole mode, indicating the value of combining classic control and learning algorithms. Moreover, we can find that although PIO behaves better than ACT in simulated environments, its success rates are lower in real robot experiments. This is caused by the slow inference of PIO. Therefore, fast inference speed is important for models used in dynamic object manipulation.

### C. Theory Verification

This subsection validates the entropy analysis framework described in Section III, *i.e.*, how the changes of observation entropy  $\mathcal{H}(\mathcal{O}_C)$  and action prediction entropy  $\mathcal{H}(\mathcal{A}_C|\mathcal{O}_C)$  affect the target distribution approximation precision. As the entropy of robotic manipulation is too complex to quantify, we design a toy task named MazeNav to study this problem. Specifically, as shown in Fig. 12 (a), a robot is initialized in a random grid of the  $5 \times 5$  maze and needs to find a path to reach the destination marked by a yellow star. The destination is always in the bottom-right corner of the maze. The action space includes moving up, down, left, and right. The robot is not allowed to move beyond the maze boundaries.

As illustrated in Fig. 12 (b), a deterministic expert policy is built to generate demonstrations. Based on the demonstrations, a student policy is to estimate the expert policy action distribution by calculating the frequency of each action taken in each state observation. If an action is never performed given a state, the student policy assigns equal possibilities to all candidate actions in this observation state.

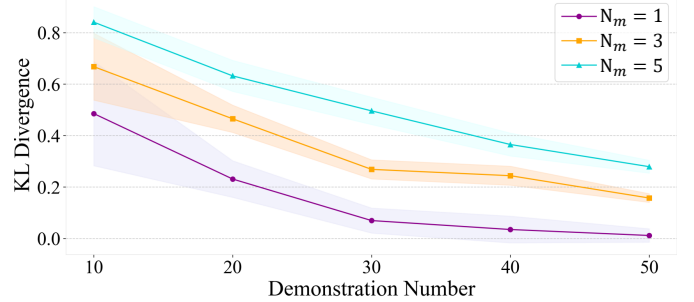


Fig. 13. This figure illustrates the relation between  $\mathcal{H}(\mathcal{O}_C)$  and the target distribution approximation precision.  $\mathcal{H}(\mathcal{O}_C)$  is adjusted by changing  $N_m$ . The approximation precision is measured by the KL divergence between the expert distribution and student distribution.

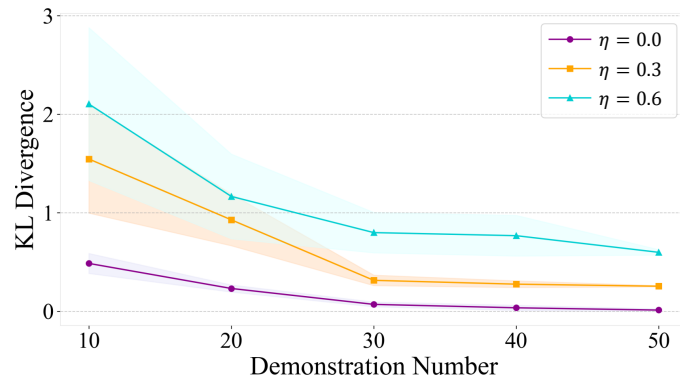


Fig. 14. This figure illustrates the relation between  $\mathcal{H}(\mathcal{A}_C|\mathcal{O}_C)$  and the target distribution approximation precision.  $\mathcal{H}(\mathcal{A}_C|\mathcal{O}_C)$  is adjusted by changing  $\eta$ . The approximation precision is measured by the KL divergence between the expert distribution and student distribution.

Besides the robot position, the state observation of the student policy includes an integer variable  $n_m$  randomly sampled from  $[1, N_m]$ . As a random variable,  $n_m$  is irrelevant to action prediction. We can change  $N_m$  to adjust  $\mathcal{H}(\mathcal{O}_C)$ . To alter  $\mathcal{H}(\mathcal{A}_C|\mathcal{O}_C)$ , we introduce a threshold variable  $\eta \in (0, 1)$ . During collecting demonstrations, if a variable sampled between  $(0, 1)$  is smaller than  $\eta$ , the action is randomly selected from the action space rather than decided by the expert policy. Hence, by increasing  $\eta$ ,  $\mathcal{H}(\mathcal{A}_C|\mathcal{O}_C)$  is enhanced.

1) *Observation Entropy Verification:* By adjusting  $N_m$  and the demonstration trajectory number, this part studies the relation between  $\mathcal{H}(\mathcal{O}_C)$  and the expert distribution approximation precision. Specifically,  $\eta$  is fixed as 0, meaning that there is no action prediction ambiguity. To study the approximation performance under various  $\mathcal{H}(\mathcal{O}_C)$  values, we repeat this experiment by setting  $N_m$  to 1, 3, and 5 separately. In each experiment, the expert policy generates 10, 20, 30, 40, and 50 demonstration trajectories to update the student policy, respectively. After the update, the expert distribution approximation precision is measured by the KL divergence between the expert and student action distributions.

To eliminate the influence of random factors, we set different seeds and repeat each experiment five times to calculate the standard deviation. The obtained KL divergence values and standard deviations under different  $N_m$  and demonstration trajectory numbers are visualized in Fig. 13. We can observe that

→	↓	→	↓	↓
↓	→	↓	→	↓
→	↓	→	↓	↓
↓	→	↓	→	↓
→	→	→	→	★

(a) The expert policy

↓	←	→	↓	↓
↓	→	→	→	↑
↓	→	→	→	→
↑	→	→	↓	↓
←	→	↑	→	★

(b) 50 demonstrations

→	↑	→	↓	↓
↓	→	←	→	↓
↑	↓	→	↓	↓
↓	↓	↓	→	↓
→	→	→	→	★

(c) 200 demonstrations

→	↓	→	↓	↓
↓	→	↓	→	↓
→	↓	→	↓	↓
↓	→	↓	→	↓
→	→	→	→	★

(d) 1000 demonstrations

Fig. 15. This experiment suggests that the student policy can perfectly estimate the action choices of the expert policy if sufficient demonstrations are provided, even though the demonstrations are very noisy (high  $\mathcal{H}(\mathcal{A}_C|\mathcal{O}_C)$ ) and contain much irrelevant observation (high  $\mathcal{H}(\mathcal{O}_C)$ ). Specifically, the subfigure (a) visualizes the expert policy. Subfigures (b)-(d) show the student policies updated with 50, 200, and 1000 demonstrations, respectively. The student policy using 1000 demonstrations perfectly replicates the expert policy.

increasing the demonstration number improves the approximation performance and is helpful in reducing the standard deviation. In addition, by increasing  $N_m$ , which means larger  $\mathcal{H}(\mathcal{O}_C)$ , the approximation precision deteriorates when using the same number of demonstrations. These observations are consistent with the theoretical analysis in Section III-C.

2) *Action Prediction Entropy Verification*: This part explores the relation between  $\mathcal{H}(\mathcal{A}_C|\mathcal{O}_C)$  and the expert distribution approximation precision. Specifically,  $N_m$  is fixed as 1, indicating that the policy observation does not include redundant information. We set  $\eta$  to 0.0, 0.3, and 0.6 separately to adjust  $\mathcal{H}(\mathcal{A}_C|\mathcal{O}_C)$ . Similar to the previous experiment, we update the policy using 10, 20, 30, 40, and 50 demonstration trajectories, respectively. The experiment of each hyperparameter is repeated five times to compute the mean KL divergence and standard deviation. The experimental results of different  $\eta$  and demonstration numbers are shown in Fig. 14.

According to the results, we can find that a larger  $\eta$ , which indicates bigger  $\mathcal{H}(\mathcal{A}_C|\mathcal{O}_C)$ , leads to poorer distribution estimation precision. In addition, by incorporating more demonstrations, the student policy can still estimate a promising expert policy distribution even though  $\eta$  is high. These results confirm the theoretical analysis in Section III-D.

3) *Effect of Data Scaling Up*: This experiment aims to validate the hypothesis in Section III-B that the optimal actions can be precisely approximated by scaling up expert demonstrations. To study this hypothesis, we set  $N_m$  to 10,

TABLE III  
COMPARISON BETWEEN POINT AND IMAGE OBSERVATIONS.

Input	Mask	Sim_in↑	Sim_out↑	Real_in↑	Real_out↑
Image	✗	0.75	0.60	0.64	0.33
Image	✓	0.41	0.28	0.38	0.14
Point	✗	0.79	0.71	0.73	0.66
Point	✓	0.87	0.78	0.85	0.74

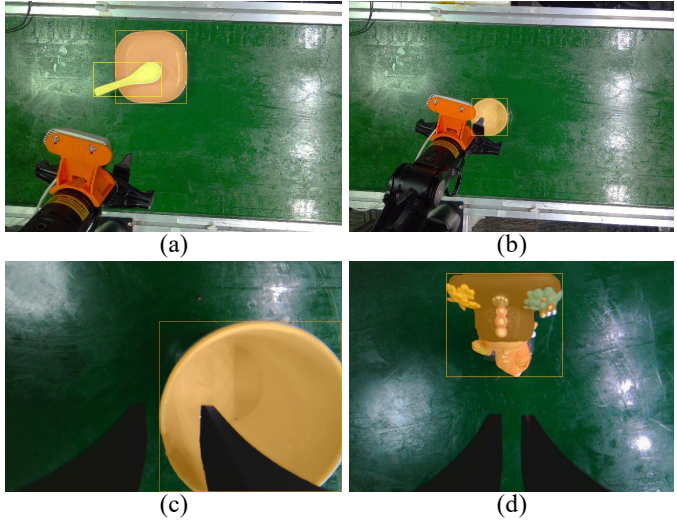


Fig. 16. This figure visualizes some instance segmentation cases during manipulation, where we can find that the segmentation masks are precise.

which leads to high  $\mathcal{H}(\mathcal{O}_C)$ . Besides,  $\eta$  is 0.9, meaning the robot performs random actions in 90% of the steps. This results in a large  $\mathcal{H}(\mathcal{A}_C|\mathcal{O}_C)$ .

We update the student policy with 50, 200, and 1000 demonstrations. Then, we visualize the student policy actions corresponding to the biggest probabilities under various states in Fig. 15 (b)-(d). We can find that even though the demonstration data is highly noisy, the student policy still perfectly replicates the expert policy using 1000 demonstrations. This result confirms the hypothesis that the optimal actions can be precisely approximated with sufficient demonstrations.

#### D. Component Analysis

This subsection ablates the various designs in GEM. Due to the space limit, when simultaneously reporting the in-domain and out-of-domain results in simulated and real environments, we report the average success rates of all skills.

1) *Analysis on Point based Representation*: Different from previous works commonly taking 2D images as input, our method utilizes 3D points. This design is based on the intuition that accurate manipulation relies on the geometry of objects, and 3D points better deliver such information. This experiment is to validate this intuition. The results are presented in Table III, where the first two rows of results correspond to the models based on images, and the last two rows are the models using points. When the input is in the image modality, the feature extractor of the recurrent probabilistic network is changed to DINoV2 [64], a widely adopted network due to its discriminative representation. The second column indicates

TABLE IV  
MANIPULATION PERFORMANCE IN VARIOUS MOVING SPEEDS.

Speed (m/s)	Pick $\uparrow$	Put $\uparrow$	Rotate $\uparrow$	Insert $\uparrow$
0.05	0.92	0.96	0.79	0.74
0.10	0.90	0.97	0.80	0.71
0.25	0.81	0.92	0.73	0.48
0.50	0.00	0.00	0.00	0.00

whether the background regions are removed based on instance segmentation results. “Sim\_in”, “Sim\_out”, “Real\_in”, and “Real\_out” refer to the average success rates in the settings of in-domain simulation, out-of-domain simulation, in-domain real world, out-of-domain real world, respectively.

According to the results, we can first find that the models taking 3D points as input outperform the ones with images, which confirms our intuition. Secondly, it is observed that the operation of removing background regions favors point based models but harms the performance of image based models. This is because when the input is an image, the model demands background texture to infer the depth of the target object. By contrast, the model does not need background since the object position has been known from 3D points.

2) *Analysis on Instance Segmentation:* The results in Table III have revealed how the operation of removing background based on instance segmentation affects manipulation success rates. This part analyzes the efficiency and robustness of our employed instance segmentation model, YOLOv11. Since the official YOLOv11 only supports segmenting objects in the categories defined in the COCO dataset [65], we need to collect a few additional instance segmentation data to enable YOLOv11 to handle our concerned categories. Thankfully, the development of SAM2 [57] makes this data collection process efficient. Specifically, based on SAM2, we only need to record a video for every concerned category of objects and click a point on each object to generate segmentation masks. In this way, obtaining tuning data totally takes several minutes. The inference speed of YOLOv11 evaluated on an RTX4090 GPU is more than 100FPS, meeting the real-time requirement.

Afterwards, to evaluate the segmentation precision of the tuned YOLOv11, we collect a dataset consisting of 1800 images for the objects shown in Fig. 11 (200 frames per object). Then, we utilize this dataset to validate the segmentation precision of YOLOv11. Following the testing protocol in COCO, YOLOv11 achieves a Mask AP of 94.5% in this dataset, suggesting that the segmentation precision YOLOv11 satisfies the manipulation task demand. Furthermore, we visualize some challenging cases in Fig. 16 during manipulation. It is found that the segmentation quality is promising.

3) *Analysis on Visual Servo tracking:* In GEM, we utilize the visual servo tracking module to convert the dynamic object manipulation problem into static object manipulation in the view of the recurrent probabilistic network. This study analyzes the tracking stability and velocity upper limit in real-world manipulation. Specifically, we adjust the conveyor belt to various speeds and make the robot hand track a moving object based on the visual servo tracking module. It is observed that the maximum stable tracking speed in simulation is

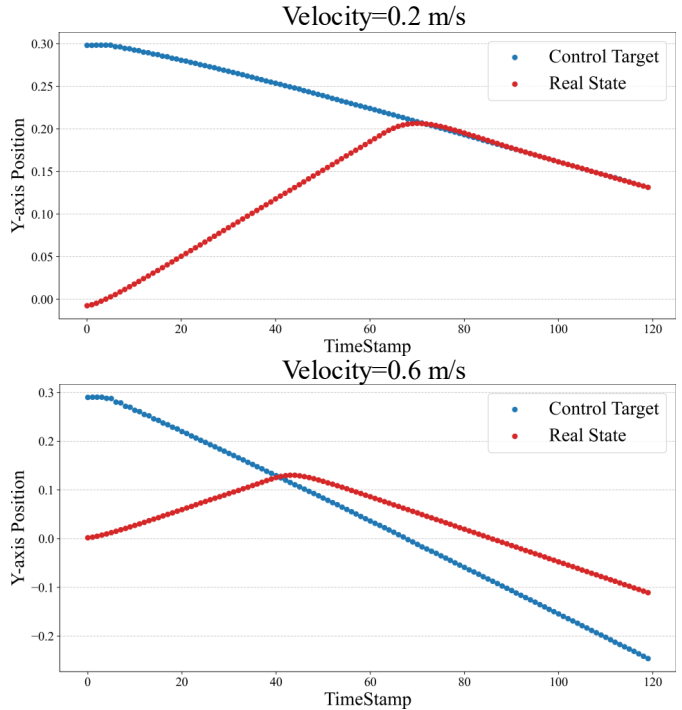


Fig. 17. This figure visualizes the tracking dynamics of the end-effector under different target velocities. We can find that the end-effector stably tracks objects moving at 0.2 m/s but fails to keep up with objects moving at 0.6 m/s.

TABLE V  
ANALYSIS ON THE EFFECT OF THE MEMORY ENCODER.

Memory	Sim_in $\uparrow$	Sim_out $\uparrow$	Real_in $\uparrow$	Real_out $\uparrow$
$\times$	0.72	0.60	0.69	0.55
$\checkmark$	0.87	0.78	0.85	0.74

approximately 0.25 m/s, and it reaches about 0.3 m/s in the real world. In Fig. 17, we visualize the dynamic curves of the control target signal and corresponding end-effector position. We can find that the end-effector approaches the moving object fast and tracks it stably under the velocity of 0.2 m/s. However, the end-effector fails to track the object when the velocity is 0.6 m/s due to its speed limit.

Afterwards, we validate the real-world success rates of GEM in the settings of different moving speeds. The results are reported in Table IV. Comparing the 1<sub>st</sub> and 2<sub>nd</sub> rows of results, we can observe that the success rates are similar when the conveyor belt runs at a low speed. When the speed is 0.25 m/s, the success rates drop due to stricter manipulation precision requirements. When the speed arrives at 0.50 m/s, the robot hand cannot perform any manipulation task because it cannot keep pace with the movement of the target object.

4) *Analysis on Memory Modeling:* As discussed in Section III-D, enabling a network to access historical memory is important for reducing action prediction ambiguity. To this end, we devise the memory encoder shown in Fig. 8. In experiments, we find that without this encoder, the robot arm could oscillate at the initial position of manipulation without approaching the target, leading to task failure. This phenomenon is more frequent when a single network learns

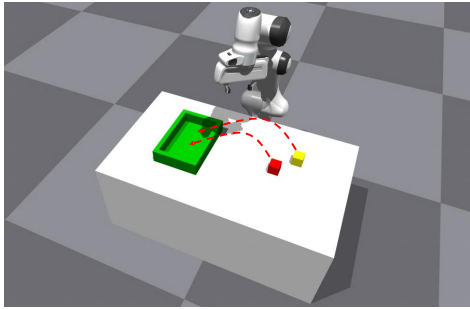


Fig. 18. This figure visualizes the simulated environment for analyzing manipulation multimodal ambiguity. During collecting demonstrations in this environment, we teleoperate the robot hand to randomly pick up one of these two blocks and put it in the green container.

TABLE VI  
ANALYSIS ON NETWORK OUTPUT.

Output	Sim_in↑	Sim_out↑	Real_in↑	Real_out↑
Direct	0.81	0.73	0.79	0.67
Probabilistic	0.87	0.78	0.85	0.74

multiple skills. This is because the policy fails to distinguish whether the manipulation operation has not started or has been completed. Our designed memory encoder can effectively address this problem by enabling the network to know which actions have been performed. We compare the performances of GEM with and without this memory encoder and report the results in Table V. According to the results, we can observe that the memory encoder significantly boosts success rates.

To more thoroughly analyze how long a sequence the memory encoder can memorize, we design a toy experiment of reciting a random digit sequence. Specifically, we update the structure of this memory encoder to support accepting a single digit as input and predicting the next digit per step. Then, we randomly generate a sequence of  $n$  digits and train the memory encoder to recite this sequence. After training, we test how many digits can be correctly recited. After repeating this experiment by setting different values of  $n$ , we find that the memory encoder can correctly recite a very long sequence like 1000 digits after sufficient epochs of training. Such a memory capability is strong enough for existing embodied policies, because current manipulation tasks usually involve at most tens of times of policy inference.

5) *Analysis on Network Output:* As explained in Section III-E, the output of the recurrent probabilistic network is a Gaussian mixture distribution to represent the predicted action probabilistic distribution. This is different from previous works that directly regress the actions to execute [18], [46]. This part analyzes the benefits of our probabilistic output.

We first compare the performances of networks based on direct action prediction and probabilistic action prediction. The results are reported in Table VI. We can observe that the recurrent probabilistic network based on probabilistic action prediction outperforms the one using direct action prediction, because the multimodal ambiguity problem is alleviated.

Notably, we argue that the results in Table VI do not sufficiently reveal the value of probabilistic action prediction. This

TABLE VII  
ANALYSIS ON HYBRID ACTION CONTROL.

Visual Servo	Sim_in↑	Sim_out↑	Real_in↑	Real_out↑
✗	0.35	0.28	0.20	0.16
✓	0.87	0.78	0.85	0.74

TABLE VIII  
ANALYSIS ON THE EFFECT OF SIMULATED DEMONSTRATIONS.

Simulated Data	Pick↑	Put↑	Rotate↑	Insert↑
✗	0.28	0.45	0.15	0.08
✓	0.92	0.96	0.79	0.74

is because the recurrent probabilistic network only observes a single target object due to the object-centric geometry perception block, and the actions in the collected demonstrations are always to manipulate this single object. There is no case like the one shown in Fig. 4, where multiple target objects appear simultaneously in the network observation.

To bridge this gap, we develop a simulated environment as shown in Fig. 18. We use the teleoperation handle shown in Fig. 5 (b) to control the robot hand to collect 50 demonstrations, where we randomly pick up one of these two blocks and put it into the green container. To study multi-target ambiguity, we remove the object-centric geometry perception block in GEM and make the recurrent probabilistic network take images as input. The feature extractor is changed to DINOv2. After training using the collected demonstrations, we compare the success rates of the networks based on direct action prediction and probabilistic action prediction. We find that the one based on direct action prediction makes the robot end-effector hover at the midpoint between the two blocks, leading to a success rate of nearly 0%. By contrast, the network based on probabilistic action prediction achieves a success rate of 87%. These results demonstrate the importance of adopting our proposed probabilistic action prediction.

6) *Analysis on Hybrid Action Control:* The hybrid action control block combines visual servo control and learnable network control to conduct dynamic object manipulation. This experiment studies how this strategy contributes to success rates compared with the common design, *i.e.*, solely based on learnable network control. The performance comparison results between GEMs with and without using the visual servo control are presented in Table VII. We can find that the visual servo control, which converts the original dynamic object manipulation problem into static manipulation, is critical for the overall task completion success rates.

7) *Analysis on Data Efficiency:* As explained in Section IV-F, since the recurrent probabilistic network takes uncolored 3D points as input, the observations in simulators become similar to real-world observations. Therefore, the simulated data can directly benefit real-world performances. Correspondingly, we collect 6,600 demonstrations in our built simulation environment. The policy trained using these simulated demonstrations should significantly favor the real-world results. To verify this issue, we compare the real-world performances of the GEM policies with and without being

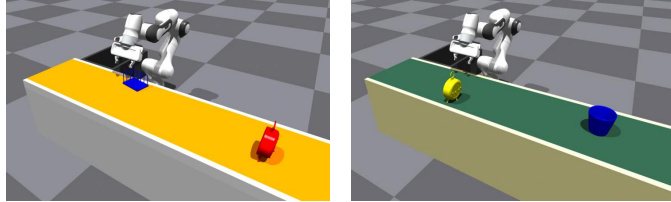


Fig. 19. To study the generalization performance of GEM across different environment backgrounds, we randomly augment the appearance of the conveyor belt, and these generated appearances are unseen in demonstrations. Two augmented samples are visualized in this figure.

TABLE IX  
ENVIRONMENT GENERALIZATION STUDY IN SIMULATION.

Environment	Pick $\uparrow$	Put $\uparrow$	Rotate $\uparrow$	Insert $\uparrow$
Seen	0.88	0.98	0.83	0.80
Unseen	0.91	0.96	0.83	0.81

pre-trained with these simulated demonstrations. Both the two policies are tuned using the 80 real-world demonstrations described in Section V-B before the real world evaluation.

The experimental results are presented in Table VIII. We can find that the simulated data boosts the success rates of various skills by large margins. According to the first row of results, only utilizing the 80 real-world demonstrations is insufficient to derive a promising policy, and collecting more real-world demonstrations is labor-intensive. Thankfully, simulated demonstrations can tackle this data scarcity problem because simulated data generation can be efficient.

### E. Generalization Analysis

The various designs in GEM are to improve the generalization of this manipulation system with minimal cost. This subsection conducts experiments to validate the generalization capabilities of GEM from different perspectives.

1) *Generalization across Environment Backgrounds:* Thanks to the rapid progress of instance segmentation [57], [66], obtaining a segmentation model meeting manipulation precision requirements has become highly cost-effective. Therefore, we design the object-centric geometry perception block in GEM that produces uncolored 3D points appended with instance IDs as the input to the recurrent probabilistic network. In this way, regardless of changes in the environment background, the input to the network remains similar. Therefore, our method should present strong generalization across different environmental backgrounds.

To validate this characteristic, we test the manipulation performance of GEM in different unseen backgrounds by changing the appearance of the conveyor belt. Since changing conveyor belts is expensive to realize in the real world, we conduct this experiment in simulation. As shown in Fig. 19, we randomly augment the colors of the conveyor belt. Since all demonstrations are collected using the conveyor belt illustrated in Fig. 9 (a), these augmented conveyor belts are unseen in demonstrations. The manipulation success rates of GEM in the original seen environment and the augmented unseen environments are presented in Table. IX. We can observe that

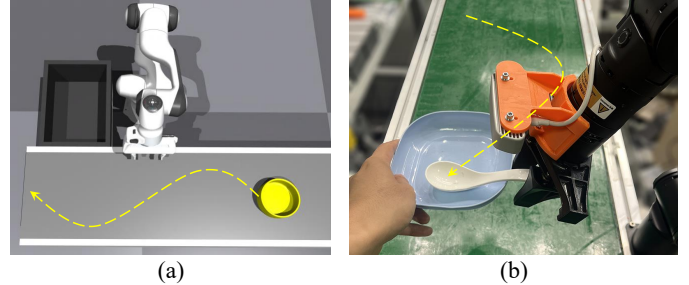


Fig. 20. This figure illustrates how we evaluate the motion pattern generalization capability of GEM in simulated and real environments. Different from the linear motion in demonstrations, in subfigure (a), the object moves following an S-shaped trajectory. In subfigure (b), the object is manually held and moves along a random curved trajectory.

TABLE X  
GENERALIZATION STUDY ON MOTION PATTERNS.

Environment	Motion	Pick $\uparrow$	Put $\uparrow$	Rotate $\uparrow$	Insert $\uparrow$
Simulated	Linear	0.88	0.98	0.83	0.80
Simulated	S-curve	0.91	0.97	0.80	0.77
Real	Linear	0.92	0.96	0.79	0.74
Real	Random curve	0.88	0.98	0.75	0.66

the performances of GEM are similar in seen and unseen environments, which is consistent with the expectation. In addition, the subsequent sim-to-real experiment in Table XIII indicates that the GEM trained using only simulated data can generalize to real-world manipulation despite the appearance gap between the simulated and real-world environments.

2) *Generalization across Motion Patterns:* As the visual servo control in the hybrid action control block transforms the original dynamic object manipulation problem into a static manipulation problem, the GEM policy should be able to generalize to manipulating objects in diverse motion patterns, *e.g.*, various moving velocities and trajectories. The experimental results in Table IV have confirmed that the manipulation success rates remain similar when the conveyor belt speed is adjusted but does not surpass the robot hand tracking velocity limit. In this experiment, we further study this problem by altering the object moving trajectories. Specifically, in simulation, we program the objects to move on the conveyor belt following an S-shaped trajectory as illustrated in Fig. 20 (a). In real-world evaluation, we manually hold a container and put the object to manipulate in this container, moving it along a random curved trajectory, as shown in Fig. 20 (b).

We report the experiment results in Table X. Comparing the performance between linear and curved object movement trajectories, we can conclude that making objects move along an unknown curved trajectory does not harm the manipulation success rates significantly. Therefore, GEM is robust to different motion patterns of moving objects.

3) *Generalization across Object Geometries:* By collecting demonstrations based on objects in diverse geometries and training the recurrent probabilistic network using these demonstrations, GEM can generalize to different geometries. The experiment results in Table I suggest that GEM can perform various manipulation skills on unseen objects with promising

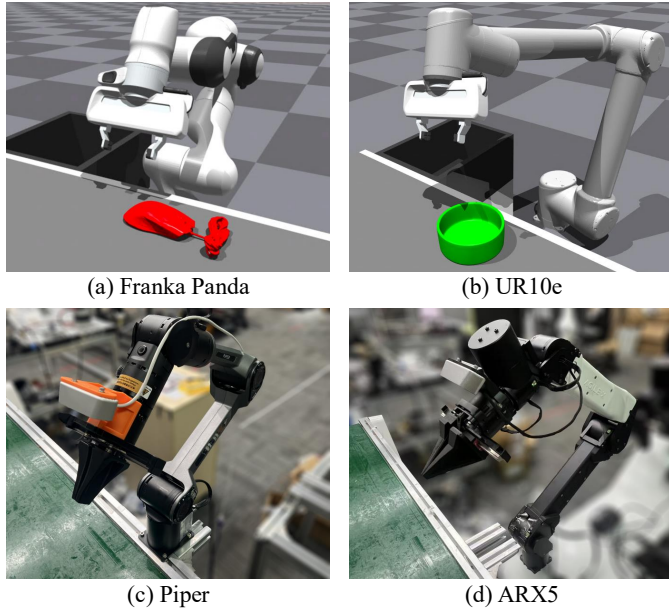


Fig. 21. This figure visualizes the four kinds of robot hands to conduct cross-embodiment evaluation in the simulated and real environments.

TABLE XI  
GENERALIZATION STUDY ON OBJECT GEOMETRIES.

Environment	Pick↑	Put↑	Rotate↑	Insert↑	Avg↑
Seen	0.92	0.96	0.79	0.74	0.85
Unseen	0.80	0.90	0.67	0.59	0.74

success rates. Table II reports the performance of GEM on manipulating seen objects in real-world tasks, where the results are similar to the ones in simulated environments. In this experiment, we further reveal the real-world success rates on manipulating the right nine unseen objects in Fig. 11. The recurrent probabilistic network validated in this experiment is the same as the one in Table II, which is first pre-trained using the 6,600 simulated demonstrations and then fine-tuned with 20 real-world demonstrations per skill.

The experiment results are reported in Table XI. We can find that although the network is only tuned with 20 demonstrations per skill, it still generalizes well to unseen objects in diverse geometries. In Section V-F, we show that if we fine-tune the network using 100 Pick demonstrations, it achieves a success rate of over 97% in an unseen application environment.

4) *Generalization across Robot Embodiments*: Thanks to the visual servo control, the end-effector moves to a fixed track position relative to the target object before that the recurrent probabilistic network begins generating manipulation actions. Additionally, the robot hand is controlled by the predicted end-effector relative offset based on inverse kinematics. Therefore, GEM is not restricted within a single robot embodiment. To evaluate the robot embodiment generalization, we conduct experiments using four kinds of robot hands in simulated and real-world environments, as shown in Fig. 21. In the simulation, the policy trained using the simulated demonstrations collected from Franka Panda is directly applied to the UR10e robot hand. In the real-world experiment, the policy tuned

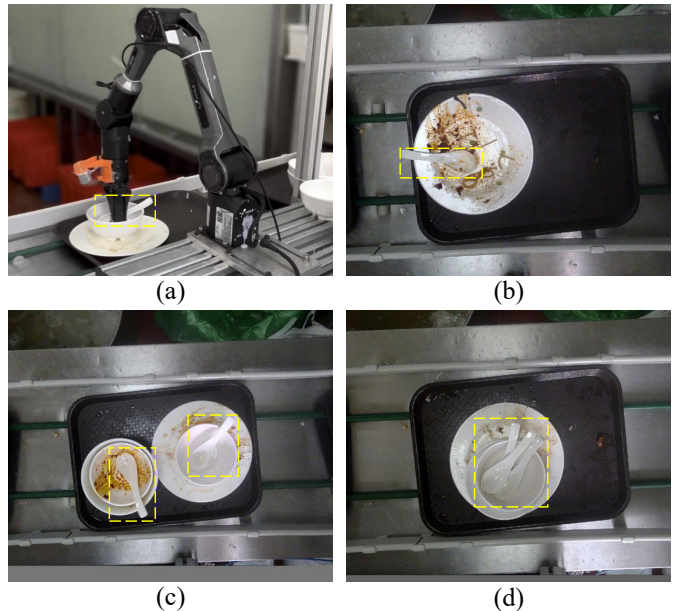


Fig. 22. Subfigure (a) shows the real application, where the robot hand needs to collect spoons from the trays moving on a conveyor belt. Subfigures (b)-(d) illustrate some challenging cases, i.e., spoons with food residue, multiple spoons to pick up within a short time window, and spoons stacked together.

TABLE XII  
GENERALIZATION STUDY ON ROBOT EMBODIMENTS.

Train	Validation	Pick↑	Put↑	Rotate↑	Insert↑
Franka	Franka	0.88	0.98	0.83	0.80
Franka	UR10e	0.91	0.97	0.85	0.79
Piper	Piper	0.92	0.96	0.79	0.74
Piper	ARX5	0.90	0.95	0.77	0.69

based on the demonstrations collected with Piper is deployed on the ARX5 robot hand to conduct manipulation.

The experiment results are reported in Table XII. It is observed that employing a robot hand to collect demonstrations and adopting another robot hand to conduct manipulation evaluation achieves similar performance compared with the setting where the demonstration collection and validation are based on the same robot hand. Hence, the robot embodiment generalization capability of GEM is confirmed.

5) *Sim-to-Real Generalization*: The input to the recurrent probabilistic network is uncolored 3D points, which do not exhibit significant differences between simulated and real environments. Therefore, GEM solely based on simulated demonstrations can generalize to the real world to perform operations. To validate this characteristic, we report the real-world manipulation success rates of GEMs with and without tuning in Table XIII. According to the results, we can observe that the GEM trained using only simulated data can manipulate objects in the real world, though its success rates are lower than the GEM tuned with 20 demonstrations per skill. Through analysis, we find this is caused by two reasons. First of all, without tuning, the test objects are all unseen in demonstrations, which increases the manipulation challenge. Secondly, in a robot control system, there is a control execution delay between the input signal and the system response. This control

TABLE XIII  
ANALYSIS ON SIM-TO-REAL GENERALIZATION.

Tune	Pick $\uparrow$	Put $\uparrow$	Rotate $\uparrow$	Insert $\uparrow$
$\times$	0.76	0.83	0.55	0.48
$\checkmark$	0.92	0.96	0.79	0.74

execution delays are different between simulated and real robots, further enhancing the difficulty.

#### F. Real Application Deployment

Different from lab environments, it is often infeasible to collect demonstrations in real application scenes because of the uninterrupted normal workflows and strict confidentiality requirements. Therefore, if a policy is to be deployed, it should be capable of operating in unseen environments with consistently high success rates, handling unexpected object poses and lighting changes. The aforementioned techniques proposed in this work help GEM meet these demands.

To evaluate the robustness of GEM, we deploy it in a canteen kitchen to conduct tableware collection. Specifically, after dining, canteen customers place their used tableware on a conveyor belt, which transports these items to the kitchen. The manipulation system needs to identify and pick out the spoons from the tableware and place them into a separate container, as shown in Fig. 22 (a). The spoons are placed in varying poses and may shift during transport. In addition, as depicted in Fig. 22 (b)-(d), other challenges include food residue obscuring spoon pose recognition, the robot arm needing to grasp and place multiple spoons within tight time windows, and spoons stacked together, etc.

Since onsite data collection is infeasible in this canteen, we teleoperate 100 demonstrations using the manipulation platform shown in Fig. 5. Then, we utilize these 100 demonstrations to fine-tune the GEM policy that has been pre-trained with the 6,600 simulated data. Finally, we deploy the fine-tuned GEM in this canteen to conduct spoon collection. We evaluate GEM over a seven-day period, processing more than ten thousand spoons, and measure a final manipulation success rate of 97.2%. This marks the first real application of imitation learning in dynamic object manipulation.

## VI. CONCLUSION

This paper has first developed an entropy-based theoretical framework to analyze the data requirements of imitation learning. Based on this framework, we have proposed GEM that reduces observation complexity and action prediction ambiguity to achieve strong generalization. Through extensive experiments, GEM has successfully generalized across diverse environment backgrounds, motion patterns, object geometries, and robot embodiments, achieving a success rate of over 97% in a real-world application without using any in-scene demonstration. These results have demonstrated that our theoretical insights effectively guide the design of an efficient manipulation system, offering a practical solution for industrial automation with reduced data costs.

## REFERENCES

- [1] N. P. Papanikolopoulos, P. K. Khosla, and T. Kanade, “Visual tracking of a moving target by a camera mounted on a robot: A combination of control and vision,” *IEEE Trans. Robotics*, vol. 9, no. 1, pp. 14–35, 1993.
- [2] E. Oztemel and S. Gursev, “Literature review of industry 4.0 and related technologies,” *J. Intell. Manuf.*, vol. 31, no. 1, pp. 127–182, 2020.
- [3] H. Kim, Y. Ohmura, and Y. Kuniyoshi, “Goal-conditioned dual-action imitation learning for dexterous dual-arm robot manipulation,” *IEEE Trans. Robotics*, 2024.
- [4] Y. Huang, N. C. Taylor, A. Conkey, W. Liu, and T. Hermans, “Latent space planning for multiobject manipulation with environment-aware relational classifiers,” *IEEE Trans. Robotics*, vol. 40, pp. 1724–1739, 2024.
- [5] M. Suomalainen, Y. Karayannidis, and V. Kyrki, “A survey of robot manipulation in contact,” *IEEE Rob. Auton. Syst.*, vol. 156, p. 104224, 2022.
- [6] S. Cobos, M. Ferre, M. S. Uran, J. Ortego, and C. Pena, “Efficient human hand kinematics for manipulation tasks,” in *IEEE/RSJ Int. Conf. Intell. Robot. and Syst.*, pp. 2246–2251, 2008.
- [7] M. Zare, P. M. Kebria, A. Khosravi, and S. Nahavandi, “A survey of imitation learning: Algorithms, recent developments, and challenges,” *IEEE Trans. Cybern.*, 2024.
- [8] T. Zhao, V. Kumar, S. Levine, and C. Finn, “Learning fine-grained bimanual manipulation with low-cost hardware,” *Robotics: Science and Systems*, 2023.
- [9] A. O’Neill, A. Rehman, A. Maddukuri, A. Gupta, A. Padalkar, A. Lee, A. Pooley, A. Gupta, A. Mandlikar, A. Jain, et al., “Open x-embodiment: Robotic learning datasets and rt-x models,” in *IEEE Int. Conf. Robot. Autom.*, pp. 6892–6903, 2024.
- [10] A. Khazatsky, K. Pertsch, S. Nair, A. Balakrishna, S. Dasari, S. Karamcheti, S. Nasiriany, M. K. Srirama, L. Y. Chen, K. Ellis, et al., “Droid: A large-scale in-the-wild robot manipulation dataset,” in *Robotics: Science and Systems*, 2024.
- [11] M. J. Kim, K. Pertsch, S. Karamcheti, T. Xiao, A. Balakrishna, S. Nair, R. Rafailov, E. P. Foster, P. R. Sanketi, Q. Vuong, et al., “Openvla: An open-source vision-language-action model,” in *Annu. Conf. Robot. Learn.*
- [12] K. Black, N. Brown, D. Driess, A. Esmail, M. Equi, C. Finn, N. Fusai, L. Groom, K. Hausman, B. Ichter, et al., “Pi0: A vision-language-action flow model for general robot control,” *arXiv preprint arXiv:2410.24164*, 2024.
- [13] Y. Zhang, R. Wang, and X. Chen, “Dynamic behavior cloning with temporal feature prediction: Enhancing robotic arm manipulation in moving object tasks,” *IEEE Robot. Autom. Lett.*, 2025.
- [14] W. Jin and M. Posa, “Task-driven hybrid model reduction for dexterous manipulation,” *IEEE Trans. Robotics*, vol. 40, pp. 1774–1794, 2024.
- [15] Z. Zhang, X. Wang, J. Liu, C. Dai, and Y. Sun, “Robotic micromanipulation: Fundamentals and applications,” *Annu. Rev. Control Robot. Auton. Syst.*, vol. 2, no. 1, pp. 181–203, 2019.
- [16] Y. LeCun, Y. Bengio, and G. Hinton, “Deep learning,” *nature*, vol. 521, no. 7553, pp. 436–444, 2015.
- [17] M. Caron, H. Touvron, I. Misra, H. Jégou, J. Mairal, P. Bojanowski, and A. Joulin, “Emerging properties in self-supervised vision transformers,” in *Int. Conf. Comput. Vis.*, pp. 9650–9660, 2021.
- [18] Z. Fu, T. Z. Zhao, and C. Finn, “Mobile aloha: Learning bimanual mobile manipulation using low-cost whole-body teleoperation,” in *Annu. Conf. Robot. Learn.*, 2024.
- [19] M. Shridhar, L. Manuelli, and D. Fox, “Perceiver-actor: A multi-task transformer for robotic manipulation,” in *Annu. Conf. Robot. Learn.*, pp. 785–799, 2023.
- [20] S. Nair, A. Rajeswaran, V. Kumar, C. Finn, and A. Gupta, “R3m: A universal visual representation for robot manipulation,” in *Annu. Conf. Robot. Learn.*, pp. 892–909, 2023.
- [21] X. Wu, L. Jiang, P.-S. Wang, Z. Liu, X. Liu, Y. Qiao, W. Ouyang, T. He, and H. Zhao, “Point transformer v3: Simpler faster stronger,” in *IEEE/CVF Conf. Comput. Vis. Pattern Recog.*, pp. 4840–4851, 2024.
- [22] C. R. Qi, H. Su, K. Mo, and L. J. Guibas, “Pointnet: Deep learning on point sets for 3d classification and segmentation,” in *IEEE/CVF Conf. Comput. Vis. Pattern Recog.*, pp. 652–660, 2017.
- [23] A. Goyal, J. Xu, Y. Guo, V. Blukis, Y.-W. Chao, and D. Fox, “Rvt: Robotic view transformer for 3d object manipulation,” in *Annu. Conf. Robot. Learn.*, pp. 694–710, PMLR, 2023.
- [24] X. Wu, X. Wen, X. Liu, and H. Zhao, “Masked scene contrast: A scalable framework for unsupervised 3d representation learning,” in *IEEE/CVF Conf. Comput. Vis. Pattern Recog.*, pp. 9415–9424, 2023.

[25] X. Wu, D. DeTone, D. Frost, T. Shen, C. Xie, N. Yang, J. Engel, R. Newcombe, H. Zhao, and J. Straub, "Sonata: Self-supervised learning of reliable point representations," in *IEEE/CVF Conf. Comput. Vis. Pattern Recog.*, pp. 22193–22204, 2025.

[26] J. Achiam, S. Adler, S. Agarwal, L. Ahmad, I. Akkaya, F. L. Aleman, D. Almeida, J. Altenschmidt, S. Altman, S. Anadkat, *et al.*, "Gpt-4 technical report," *arXiv preprint arXiv:2303.08774*, 2023.

[27] S. Liu, L. Wu, B. Li, H. Tan, H. Chen, Z. Wang, K. Xu, H. Su, and J. Zhu, "Rdt-1b: a diffusion foundation model for bimanual manipulation," 2025.

[28] J. Bjorck, F. Castañeda, N. Cherniadev, X. Da, R. Ding, L. Fan, Y. Fang, D. Fox, F. Hu, S. Huang, *et al.*, "Gr0ot n1: An open foundation model for generalist humanoid robots," *arXiv preprint arXiv:2503.14734*, 2025.

[29] K. Ehsani, T. Gupta, R. Hendrix, J. Salvador, L. Weihs, K.-H. Zeng, K. P. Singh, Y. Kim, W. Han, A. Herrasti, *et al.*, "Spoc: Imitating shortest paths in simulation enables effective navigation and manipulation in the real world," in *IEEE/CVF Conf. Comput. Vis. Pattern Recog.*, pp. 16238–16250, 2024.

[30] J. Matas, S. James, and A. J. Davison, "Sim-to-real reinforcement learning for deformable object manipulation," in *Annu. Conf. Robot. Learn.*, pp. 734–743, 2018.

[31] E. Todorov, T. Erez, and Y. Tassa, "Mujoco: A physics engine for model-based control," in *IEEE/RSJ Int. Conf. Intell. Robot. and Syst.*, pp. 5026–5033, 2012.

[32] V. Makoviychuk, L. Wawrzyniak, Y. Guo, M. Lu, K. Storey, M. Macklin, D. Hoeller, N. Rudin, A. Allshire, A. Handa, and G. State, "Isaac gym: High performance gpu based physics simulation for robot learning," in *Adv. Neural Inform. Process. Syst.*, vol. 1, 2021.

[33] S. Nambiar, M. Jonsson, and M. Tarkian, "Automation in unstructured production environments using isaac sim: A flexible framework for dynamic robot adaptability," *Procedia CIRP*, vol. 130, pp. 837–846, 2024.

[34] D. Kalashnikov, A. Irpan, P. Pastor, J. Ibarz, A. Herzog, E. Jang, D. Quillen, E. Holly, M. Kalakrishnan, V. Vanhoucke, *et al.*, "Scalable deep reinforcement learning for vision-based robotic manipulation," in *Annu. Conf. Robot. Learn.*, pp. 651–673, 2018.

[35] S. Deng, M. Yan, S. Wei, H. Ma, Y. Yang, J. Chen, Z. Zhang, T. Yang, X. Zhang, H. Cui, *et al.*, "Graspvla: a grasping foundation model pre-trained on billion-scale synthetic action data," *arXiv preprint arXiv:2505.03233*, 2025.

[36] B. Tang, I. Akinola, J. Xu, B. Wen, A. Handa, K. Van Wyk, D. Fox, G. S. Sukhatme, F. Ramos, and Y. Narang, "Automate: Specialist and generalist assembly policies over diverse geometries," in *Robotics: Science and Systems*, 2024.

[37] H.-S. Fang, C. Wang, H. Fang, M. Gou, J. Liu, H. Yan, W. Liu, Y. Xie, and C. Lu, "Anygrasp: Robust and efficient grasp perception in spatial and temporal domains," *IEEE Trans. Robotics*, vol. 39, no. 5, pp. 3929–3945, 2023.

[38] R. Wang, J. Zhang, J. Chen, Y. Xu, P. Li, T. Liu, and H. Wang, "Dexgraspnet: A large-scale robotic dexterous grasp dataset for general objects based on simulation," in *IEEE Int. Conf. Robot. Autom.*, pp. 11359–11366, 2023.

[39] R. Han, S. Wang, S. Wang, Z. Zhang, J. Chen, S. Lin, C. Li, C. Xu, Y. C. Eldar, Q. Hao, *et al.*, "Neupan: Direct point robot navigation with end-to-end model-based learning," *IEEE Trans. Robotics*, 2024.

[40] L. Zhuoling, R. Liangliang, Y. Jinrong, Z. Yong, *et al.*, "Vip: Vision instructed pre-training for robotic manipulation," *Proc. Int. Conf. Mach. Learn.*, 2025.

[41] R. Rombach, A. Blattmann, D. Lorenz, P. Esser, and B. Ommer, "High-resolution image synthesis with latent diffusion models," in *IEEE/CVF Conf. Comput. Vis. Pattern Recog.*, pp. 10684–10695, 2022.

[42] B. Zitkovich, T. Yu, S. Xu, P. Xu, T. Xiao, F. Xia, J. Wu, P. Wohlhart, S. Welker, A. Wahid, *et al.*, "Rt-2: Vision-language-action models transfer web knowledge to robotic control," in *Annu. Conf. Robot. Learn.*, 2023.

[43] A. Wang, A. Singh, J. Michael, F. Hill, O. Levy, and S. R. Bowman, "Glue: A multi-task benchmark and analysis platform for natural language understanding," in *Int. Conf. Learn. Represent.*

[44] C. E. Shannon, "A mathematical theory of communication," *The Bell system technical journal*, vol. 27, no. 3, pp. 379–423, 1948.

[45] L. X. Shi, Z. Hu, T. Z. Zhao, A. Sharma, K. Pertsch, J. Luo, S. Levine, and C. Finn, "Yell at your robot: Improving on-the-fly from language corrections," in *Robotics: Science and Systems*, 2024.

[46] C. Chi, Z. Xu, S. Feng, E. Cousineau, Y. Du, B. Burchfiel, R. Tedrake, and S. Song, "Diffusion policy: Visuomotor policy learning via action diffusion," *Int. J. Robot. Res.*, p. 02783649241273668, 2023.

[47] R. Geirhos, J.-H. Jacobsen, C. Michaelis, R. Zemel, W. Brendel, M. Bethge, and F. A. Wichmann, "Shortcut learning in deep neural networks," *Nature Machine Intelligence*, vol. 2, no. 11, pp. 665–673, 2020.

[48] Y. Liu, J. Yan, F. Jia, S. Li, A. Gao, T. Wang, and X. Zhang, "Petriv2: A unified framework for 3d perception from multi-camera images," in *Int. Conf. Comput. Vis.*, pp. 3262–3272, 2023.

[49] S. Hochreiter and J. Schmidhuber, "Long short-term memory," *Neural computation*, vol. 9, no. 8, pp. 1735–1780, 1997.

[50] Q. Yang, W.-N. Chen, Y. Li, C. P. Chen, X.-M. Xu, and J. Zhang, "Multimodal estimation of distribution algorithms," *IEEE Trans. Cybern.*, vol. 47, no. 3, pp. 636–650, 2016.

[51] A. G. Barnett, J. C. Van Der Pols, and A. J. Dobson, "Regression to the mean: what it is and how to deal with it," *Int. J. Epidemiol.*, vol. 34, no. 1, pp. 215–220, 2005.

[52] D. A. Reynolds *et al.*, "Gaussian mixture models," *Encyclopedia of biometrics*, vol. 741, no. 659-663, p. 3, 2009.

[53] S. KuCuk and Z. Bingul, "The inverse kinematics solutions of industrial robot manipulators," in *Proc. IEEE Int. Conf. Mechatronics*, pp. 274–279, 2004.

[54] L. Yang, B. Kang, Z. Huang, X. Xu, J. Feng, and H. Zhao, "Depth anything: Unleashing the power of large-scale unlabeled data," in *IEEE/CVF Conf. Comput. Vis. Pattern Recog.*, pp. 10371–10381, 2024.

[55] B. Wen, M. Trepte, J. Aribido, J. Kautz, O. Gallo, and S. Birchfield, "Foundationstereo: Zero-shot stereo matching," in *IEEE/CVF Conf. Comput. Vis. Pattern Recog.*, 2025.

[56] R. Khanam and M. Hussain, "Yolov11: An overview of the key architectural enhancements," *arXiv preprint arXiv:2410.17725*, 2024.

[57] N. Ravi, V. Gabeur, Y.-T. Hu, R. Hu, C. Ryali, T. Ma, H. Khedr, R. Rädel, C. Rolland, L. Gustafson, *et al.*, "Sam 2: Segment anything in images and videos," *arXiv preprint arXiv:2408.00714*, 2024.

[58] C. Williams and C. Rasmussen, "Gaussian processes for regression," *Adv. Neural Inform. Process. Syst.*, vol. 8, 1995.

[59] N. Carion, F. Massa, G. Synnaeve, N. Usunier, A. Kirillov, and S. Zagoruyko, "End-to-end object detection with transformers," in *Eur. Conf. Comput. Vis.*, pp. 213–229, 2020.

[60] L. Downs, A. Francis, N. Koenig, B. Kinman, R. Hickman, K. Reymann, T. B. McHugh, and V. Vanhoucke, "Google scanned objects: A high-quality dataset of 3d scanned household items," in *IEEE Int. Conf. Robot. Autom.*, pp. 2553–2560, 2022.

[61] I. Loshchilov and F. Hutter, "Decoupled weight decay regularization," in *Int. Conf. Learn. Represent.*, 2017.

[62] T. Zhang, Z. McCarthy, O. Jow, D. Lee, X. Chen, K. Goldberg, and P. Abbeel, "Deep imitation learning for complex manipulation tasks from virtual reality teleoperation," in *IEEE Int. Conf. Robot. Autom.*, pp. 5628–5635, 2018.

[63] A. Goyal, V. Blukis, J. Xu, Y. Guo, Y.-W. Chao, and D. Fox, "Rvt-2: Learning precise manipulation from few demonstrations," in *Robotics: Science and Systems*, 2024.

[64] M. Oquab, T. Darcret, T. Moutakanni, H. Vo, M. Szafraniec, V. Khalidov, P. Fernandez, D. Haziza, F. Massa, A. El-Nouby, *et al.*, "Dinov2: Learning robust visual features without supervision," *Trans. Mach. Learn. Res.*, pp. 1–31, 2024.

[65] T.-Y. Lin, M. Maire, S. Belongie, J. Hays, P. Perona, D. Ramanan, P. Dollár, and C. L. Zitnick, "Microsoft coco: Common objects in context," in *Eur. Conf. Comput. Vis.*, pp. 740–755, 2014.

[66] T.-Y. Pan, Q. Liu, W.-L. Chao, and B. Price, "Towards open-world segmentation of parts," in *IEEE/CVF Conf. Comput. Vis. Pattern Recog.*, pp. 15392–15401, 2023.